Fall 12-18-2014

# Investigation of the Quenching Characteristics of Steel Components by Static and Dynamic Analyses

Pratik Sarker
psarker1@uno.edu

# Investigation of the Quenching Characteristics of Steel Components by Static and Dynamic Analyses

A Thesis

Submitted to the Graduate Faculty of the
University of New Orleans
in partial fulfillment of the
requirements for the degree of

Master of Science
in
Engineering-Mechanical
Solid Mechanics

by

Pratik Sarker

B.Sc., Bangladesh University of Engineering and Technology, 2007

December, 2014

# DEDICATION

To

**My Father**

who taught me never to lose hope and always try to the end without expecting anything for earning an honest living

and

**My Mother**

who always encouraged me to listen to my mind to do things as I think is good and to have faith on me

# ACKNOWLEDGMENT

First of all, I would like to express my sincere gratitude to my advisor, Dr. Uttam K Chakravarty for the continuous support of my Master's study and research, for his patience, motivation, enthusiasm, and immense knowledge. I am especially thankful for his guidance on fostering my professional problem-analyzing, problem-solving, and reporting skills. His guidance helped me in all the time of research and writing of this thesis.

Besides my advisor, I would like to thank the rest of my thesis committee; Dr. Paul J Schilling and Dr. Martin J Guillot for their encouragement, insightful comments, and hard questions. I am also grateful to Dr. Kazim M Akyuzlu and Dr. David Hui for their valuable advice and guidance.

I thank my fellow labmates in University of New Orleans Computational Solid Mechanics Group; Manohar Chidurala and Jose Enrique Rubio for the stimulating discussions, for the sleepless nights we worked together before deadlines, and for all the fun we have had in the last two years.

Last but not the least, I would like to thank my family; my parents Sribash Chandra Sarker and Dharitri Sarker for giving birth to me at the first place and supporting me throughout my life.

# Table of Contents

# List of Figures

# List of Tables

# ABSTRACT

Machine components made of steel are subjected to heat treatment processes for improving mechanical properties in order to enhance product life and is usually done by quenching. During quenching, heat is transferred rapidly from the hot metal component to the quenchant and that rapid temperature drop induces phase transformation in the metal component. As a result, quenching generates some residual stresses and deformations in the material. Therefore, to estimate the temperature distribution, residual stress, and deformation computationally; three-dimensional finite element models are developed for two different steel components – a spur gear and a circular tube by a static and a dynamic quenching analyses, respectively. The time-varying nodal temperature distributions in both models are observed and the critical regions are identified. The variations of stress and deformation after quenching along different pathways for both models are studied. The convergence for both models is checked and validations of the models are done.



**Keywords:** Quenching process; finite element; fluid-structure interaction; temperature distribution; residual stress; deformation

# 1. Introduction

## 1. 1 Scope of Quenching

The application of quenching, an essential heat treatment process for hardening materials in industrial and mechanical fields, is continuously increasing worldwide for developing desired material properties. From industrial sector to most common use of alloy materials in automotive, aircraft, heavy machineries, transmission systems, engine components, etc., quenching is involved as a part of the heat treatment process. Highly loaded gears and shafts, such as those in transport or racing vehicles or a heavy duty power transmission mechanism should have fracture toughness and fatigue strength values two or three times those of conventional vehicles or mechanisms to resist failure. Therefore, they need to be quenched to serve the aforesaid purpose. In military, aircraft, and naval applications quenched steel plates are used for making dies for extrusions, nozzles, armor plates, tempered steel bars, deep drawn objects, ship hulls, and many other parts. Likewise, mechanisms that use moving parts where strength and fatigue resistance is very important, quenching can essentially ensure the necessary material properties.

This work studies heat transfer, residual and thermal stress, and distortion analysis after quenching of two steel parts – a spur gear and a circular tube by a static and a dynamic analyses, respectively. The static analysis uses a constant heat transfer coefficient while the dynamic analysis uses the fluid flow by three liquid quenchants; water, brine, and propylene glycol (PG).

## 1.2 Mechanism of Quenching: A Typical Heat Treatment Process

Heat treatment is a method mainly used to alter the physical properties such as microstructure, mechanical behavior; and sometimes chemical properties such as carbon

concentration of a material or a part. Unlike grinding and machining, there is usually no material removal in heat treatment processes. Typical heat treatment processes include those altering physical properties, e.g., quenching, tempering, aging, annealing, and normalizing and also those involving chemical property changes, e.g., carburizing and nitriding.

In material science, quenching is a heat treatment process, in which it is cooled rapidly from its austenitization temperature. It prevents low-temperature processes such as phase transformations from occurring by only providing a narrow window of time in which the reaction is both thermodynamically favorable and kinetically accessible. Quenching is generally done for metals that are alloyed with small amounts of other metals, mostly done with steels, an alloy of iron and carbon. The temperature of steel parts from which cooling starts usually ranges from 815–900 °C. The way quenching works to harden steels is by introducing martensite, a very hard form of steel crystalline structure. Fig. 1.1 shows a schematic time-temperature-transformation (TTT) diagram [1] for the eutectoid plain carbon steel.

At high temperature, the alloying metals are dissolved in the base metal. If the material is cooled slowly, the alloy elements have time to precipitate out separately. However, if the metal is quenched, the alloying metals are trapped within the crystal grains which make it harder. At a temperature of around 750 °C, iron has a body centered cubic (BCC) structure, called ferrite. The carbon atoms can easily be held within this less tightly packed structure in what is called a solid solution. If the steel is cooled slowly, the iron atoms rearrange into a face centered cubic (FCC) structure, called austenite. The iron atoms are more tightly packed in this arrangement and cannot hold as many carbon atoms within the structure. The remaining carbon forms a compound with iron called iron carbide or cementite. If the same steel is quenched rather than being cooled slowly, the carbon atoms do not have time to form cementite. They are trapped within a ‘frozen’

austenite structure in an arrangement called martensite, generated due to the rapid phase transformation while quenching. The movement of dislocations is very difficult in this structure so the metal becomes very hard and brittle.

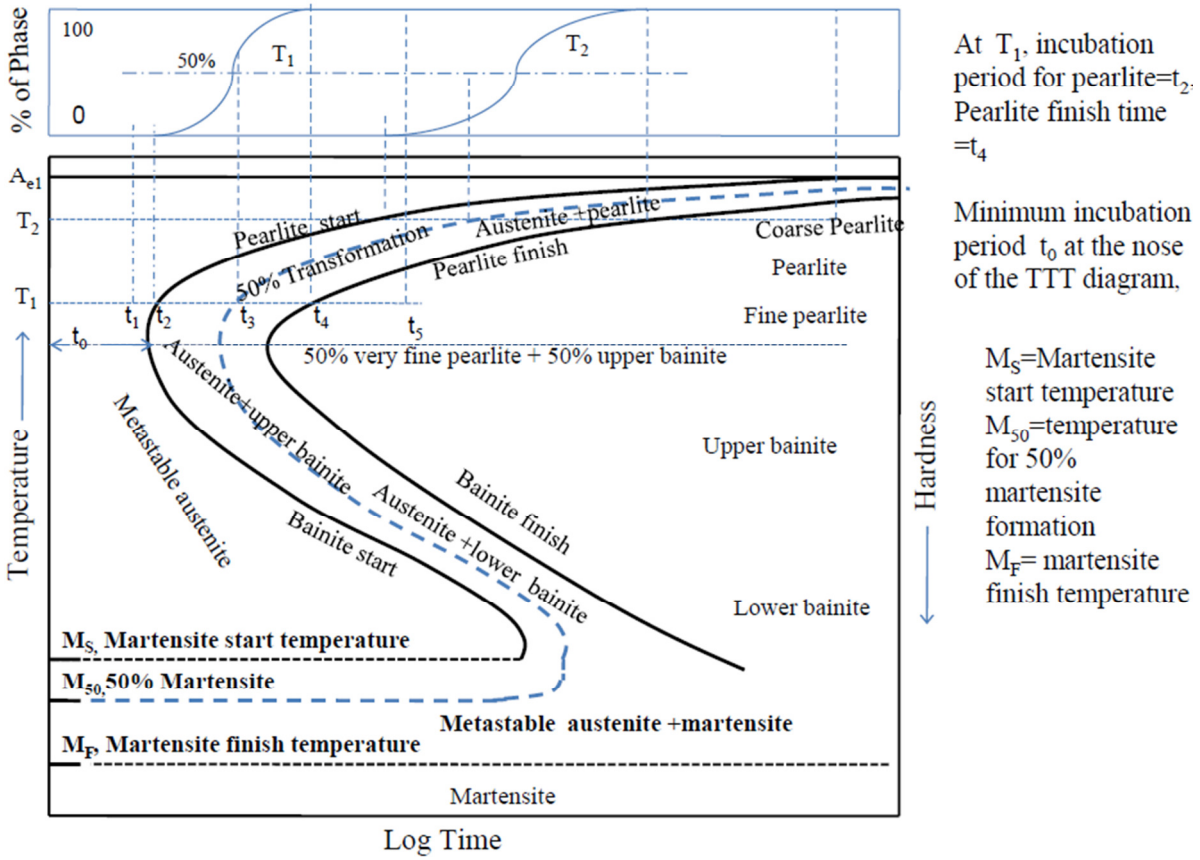


Figure 1.1: A sample TTT diagram for plain carbon eutectoid steel

Figure 1.2 illustrates some phases for steel components at different cooling rates. From Fig. 1.2, martensitic reaction begins during cooling when the austenite reaches the martensite start temperature $M_s$ and the parent austenite becomes mechanically unstable. As the sample is quenched, an increasingly large percentage of the austenite transforms to martensite until the lower transformation temperature $M_f$ is reached, at which the transformation is completed. One of the differences between the two phases is that martensite has a body centered tetragonal crystal structure, whereas austenite has a FCC structure.

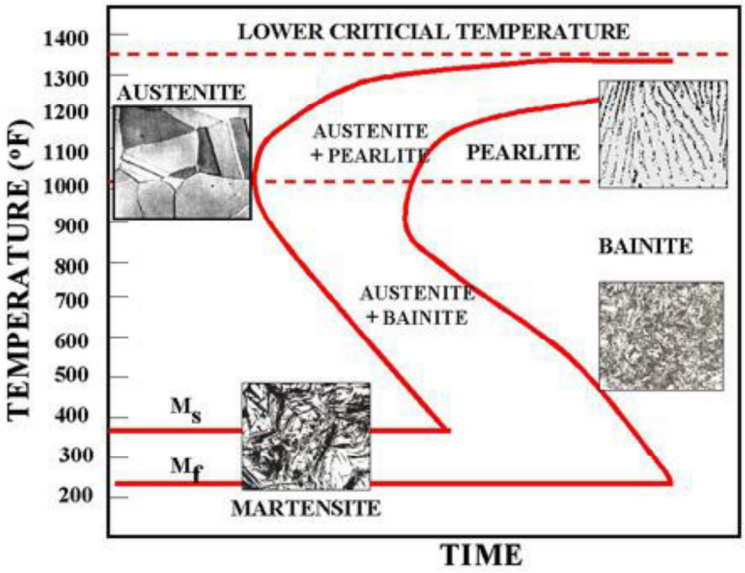


Figure 1.2: A sample TTT diagram with different microstructures

Besides improving mechanical properties, quenching produces some residual stresses in the material too, which ultimately cause deformations and increase with increasing steel hardenability. Therefore, it is necessary for the heat treaters to optimize the component design and the heat treating processes. It is important to note that the hardness is not uniform in the material after quenching and a hardness gradient exists throughout the material. The final hardness is dependent on the amount of carbon in the steel. The depth of hardness depends on the hardenability of the steel as well as the quench severity. The performance capability of the quenched part is defined by its properties (mechanical, physical, and metallurgical), which are in turn determined by the part microstructure.

## 1.3 Literature Review

As quenching is a much accelerated cooling process, it brings the metal back to room temperature, preventing the lower temperatures through which the material is cooled from having a chance to cause significant alterations in the microstructure by diffusion. The slower the

quenching rate, the longer the thermodynamic forces have a chance to alter the microstructure, which is in some cases is desirable. Hence there are uses of different quenching media either liquids like oil, water, etc., or gases. Elkatatny et al. [2] used a transient flow model aided by computational fluid dynamics (CFD) to simulate the process of high pressure gas quenching of a large die in order to predict the temperature distribution. Totten et al. [3] discussed the vapor blanket and nucleate boiling stage of heat transfer of a hot object when quenched in fluids like oil or water. Jintang et al. [4] analyzed the quenching process of a heavy rail to obtain the time varying temperature fields by simulating the different stages of heat treatment using the finite element software, ANSYS. For a rapid quenching process, the quenchant must produce enough quench severity to have martensitic transformation. A very common method for that purpose is to use liquid quenchants. Water and brine [3–7] are two such conventional liquid quenchants used for rapid cooling. While water quenching results in the formation of hard martensitic microstructure and subsequently provides high strength and toughness after tempering, it also has a tendency to create distortion and cracking in the specimen. On the other hand, brine is somewhat corrosive in nature. Oil quenching does not have these problems, but cannot provide sufficient cooling rate to harden the part as required to achieve acceptable mechanical properties, especially in large cross sections. To overcome these disadvantages of quenching by water, brine, and oil; polymeric solutions are introduced as the substitutions. There are several commercial polymer quenchants that are readily accepted and used nowadays among which glycol based quenchants are frequently used [8].

Previous works suggest that the residual stress and deformation are measured by various methods for conventional and simple geometries in transient stress analysis. Yamada [9] presented a method for solving uncoupled quasi-static thermo-elastic problems in perforated

plates with prescribed temperatures. The transient thermal stress problem in a thermally and elastically orthotropic rectangular slab was investigated by Wang and Chou [10]. Nowadays, the finite element (FE) method, one of the most powerful numerical methods, is used to predict the residual and thermal stress in the material. Toparli and Aksoy [5] analyzed the residual stress developed during water quenching of cylindrical solid steel bars of various diameters using FE method to find the transient temperature distribution in the bar. Transient temperature and residual stress fields were carried out by Fa-rong and Shang-li [11] by ADINA/ADINAT program for a metal specimen during quenching. The commercial FE software, DEFORM-HT was used to predict the material response for optimizing the gas quenching process in order to minimize the distortion [12]. Residual stresses in a large circular disk caused by local heating and cooling at its center was calculated by Gurney [13]. Several researchers [14–17] showed that the FE method could be used to simulate the real processes by comparing the results with some experimental data. Numerical investigation of the thermal stress suggested a good validation of the experimental results [18–19].

The residual stress and deformation created by quenching are influenced by a number of parameters and vice versa. Sedighi and McMahon [20] investigated the effect of variation in part orientation and quenchant circulation during quenching of steel parts to estimate the residual stresses. The residual stress generated after quenching was used to find the impact on fatigue life in an automotive aluminum alloy by using local stress and idealized pore size in the alloy [21]. Rapid tension tests were performed on the alloy in super-saturated solution state to study the development of residual stress and deformation during quenching of an aluminum alloy at several temperatures and strain rates to determine the parameters in the thermo-mechanical constitutive model [22]. Henriksen et al. [23] investigated the distortion and residual stress

accurately in carburized and quenched gear steels to show that distortions were quite sensitive to small variations in constitutive parameters. The application of new multiphase material model for simulating deformation and residual stress in carburized and quenched gear steels was also developed [24]. Different techniques for the measurement of the residual stress like optical strain rosette, resistance strain rosette, X-ray, neutron diffraction, etc., were used in the experimental study of residual stress distributions in aluminum castings after water quenching [25].

When quenched, a significant amount of residual stress is developed in the component, particularly in water [2, 21–22, 26–28] and the relevant previous works suggests some ways to minimize it. The commercial finite element software, DEFORM-HT, was used to predict the material response during the quenching process to optimize the gas quenching process in order to minimize the distortion [12]. Residual stress differences were experimented between water and air quenched aluminum castings to find significantly reduced residual stress for air quenching compared to water quenching [28]. Better control over quenching by changing fluid pressure, speed, flow direction, or the fluid itself enables absolute repeatability, optimized part microstructure, enhanced mechanical properties, and reduced manufacturing costs. Kavalco et al. [29] discussed the strength, cooling rate and intergranular corrosion of aluminum alloys with residual stress or deformation for optimization of the gas quenching efficiency. The heat transfer coefficient between the hot part and the quenchent affects the quenching result significantly. Xiao [19] studied the effect of distribution of heat transfer coefficient on the accuracy of thermal boundary conditions by numerical modeling and experimental investigation for optimization in quenching processes of aluminum and steel components. Mitchell [30] studied quenching of wrought 7075 aluminum alloy by calculating the variable heat transfer coefficient to maximize the mechanical properties without causing residual stress.

## 1.4 Research Objective

This work is dedicated to study the thermal behavior and mechanical response of two different steel parts during the quenching process by static and dynamic analyses. Specifically, the aims of this work are as follows:

**1. Heat Transfer Modeling:** At first, the heat transfer model needs to be developed in order to generate the temperature-time history of the steel part after quenching. In the static analysis, two different approaches are followed. One is the fully coupled analysis (also called coupled-temperature-displacement analysis) and another is the sequentially coupled analysis. For fully coupled analysis, the temperature-time history is developed at an instant and immediately applied to determine the corresponding stress and deformation at that instant. In the sequentially coupled analysis, the temperature-time history is developed for the whole part at the first step and is used as an input to determine the stress and deformation in the second step. In the dynamic analysis, a fluid-structure interaction (FSI) model is developed and sequentially coupled analysis is used which uncouples the thermal response from the mechanical response.

**2. Stress and Deformation Modeling:** The temperature-time history developed in both the static (sequentially coupled analysis) and dynamic analyses is used to calculate three-dimensional (3-D) stress and deformation in both steel parts. The time-varying stress and deformation at a specific point and the variation of stress and deformation along particular pathways in the steel components are determined.

The sequence of the first two steps is summarized more clearly in Fig. 1.3. Results are obtained after validation of the model is done. The convergence of the results for both analyses is ensured in terms of either temperature or stress.

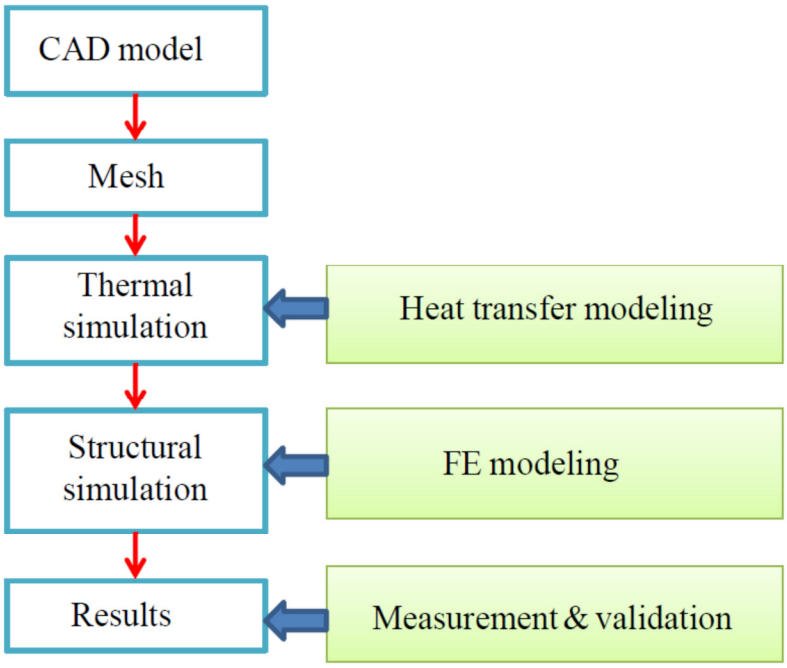


Figure 1.3: Flow chart of numerical modeling

**3. Identification of the Critical Regions:** Once the results are obtained, identification of the regions of the steel parts in both analyses after quenching is done where the stress and the deformation are the maximum.

**4. Selection of the Proper Quenchant:** In the dynamic analysis, the cooling rates for all the quenchants are compared and the criteria for selecting a suitable quenchant among different quenchants for a specific purpose are determined.

# 2. Static Quenching Analysis of a Spur Gear

## 2.1 Scope of Quenching of a Spur Gear

Spur gear quenching is done basically to make them suitable for machining into a particular shape and for withstanding high dynamic stress for a particular service. To control the deformation and achieve repeatable dimensional tolerances, the gear needs suitable constraints during the quenching cycle of the heat treatment process. Although heat treating represents a significant portion (≈ 30%) of a typical gear manufacturing cost, quenching is essentially important for spur gears to make them harder and tougher as part of the manufacturing process. This is because spur gears are the most common parts to withstand high dynamic bending and compressive stresses. They must be capable of resisting frictional wear and should have enhanced toughness for which sufficient strength is required for better performance and longer life. To meet all these requirements, the gear must be heat treated. The geometry of the gear is one of the governing factors to perform well in its service. So, it needs to be in a state or shape in which minimum amount of residual stress and deformation take place. Therefore, after quenching, identification of high stress developing regions in the gear is necessary and those regions need to be carefully designed by considering important design parameters like strength, cost, durability, and reliability.

## 2.2 Description of the Spur Gear

The object of analysis here is a steel spur gear and is symmetric about X-, Y-, and Z-axes shown in Fig. 2.1. The gear has 16 teeth. The outer circle, pitch circle, base circle, and root circle diameters are 28.6 mm, 25.4 mm, 24.6 mm, and 21.8 mm, respectively. The height and the pressure angle are 12.7 mm and 14.5°, respectively. The dimensions of the spur

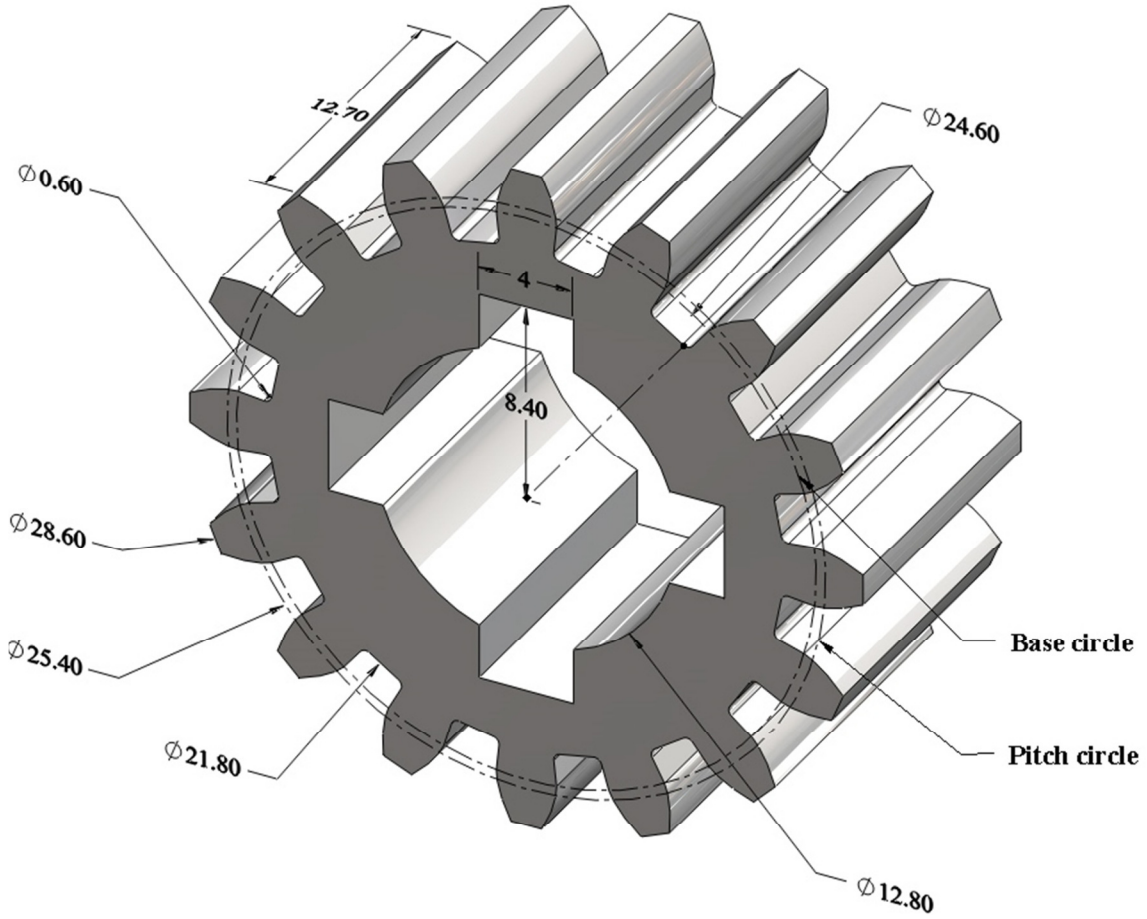


Figure. 2.1: Detailed 3-D model of the full spur gear

gear are taken from the Boston gear catalog [31]. All the gear teeth have involute profile and standard procedures are followed to maintain the involute profile of each tooth using 13 points [32]. For serving the purpose of an industrial gear, four keyways, symmetric about X-, Y-, and Z-axes are modeled around the bore hole of the spur gear. The bore diameter is 12.8 mm. The height of a key slot is 8.4 mm from the center of the bore hole and total width of the key slot is 4 mm. At the root of each tooth, a fillet of radius 0.3 mm is maintained.

## 2.3 Properties of Steel

The mechanical and thermal properties of steel are given in Table 2.1. It is assumed that the properties are isotropic and the steel is homogeneous.

Table 2.1: Physical and thermal properties of steel

| Material | Density, $kg/m^3$ | Young's modulus, Pa | Poisson's ratio | Thermal conductivity, W/m·K | Specific heat, J/kg·K | Coefficient of thermal expansion, $K^{-1}$ |
|---|---|---|---|---|---|---|
| Steel | 7800 | 207e9 | 0.3 | 50 | 500 | 0.000013 |

## 2.4 Temperature Dependence of the Yield Stress of Steel

The gear is assumed to be made of an elastic, perfectly plastic steel with the yield stress that drops linearly with temperature above 121 °C [18]. The transient stress is large enough to cause significant plastic flow, so residual stress will remain after the plate is cooled to the sink temperature. The relationship between the temperature dependent yield stress and the corresponding temperature [18] is given below by the Eqs. 2.1 and 2.2. From Eq. 2.1, when the temperature of the steel is below or not more than 121 °C, it does not affect the yield stress at all. But at very high temperature, in general, the yield stress of the steel gets reduced significantly as indicated by Eq. 2.2. The range of values for the temperature dependent yield stress and the corresponding temperature for the static model of the gear is described in Table 2.2.

$$\text{Yield stress, } Y = 248 \text{ MPa} \qquad \text{Temperature, } T \leq 121\ ^\circ\text{C} \quad (2.1)$$

$$\text{Yield stress, } Y = 248(1 - (T - 121)/1111.1) \text{ MPa} \qquad \text{Temperature, } T > 121\ ^\circ\text{C} \quad (2.2)$$

Table 2.2: Temperature dependent yield stress of steel

| Yield stress, MPa | Strain | Temperature, °C |
|---|---|---|
| 248 | 0 | 0 |
| 248 | 0 | 121 |
| 85 | 0 | 850 |
| 27 | 0 | 1111.1 |

## 2.5 Finite Element Model

Due to the symmetry about the X-, Y-, and Z-axes, a 3-D FE model of the quarter of the full spur gear is developed for investigating the thermal stress and deformation using the FE analysis software, Abaqus 6.13 [33]. The analysis is run in a transient mode and in two methods – the fully coupled and the sequentially coupled analyses. The fully coupled analysis is done by creating a coupled-temperature-displacement step. In this step, both the heat transfer and the thermal stress are interrelated. On the other hand, the sequentially coupled analysis is achieved by two stages; at first, the analysis is run as a pure heat transfer step to get the temperature-time history until the model is cooled. Secondly, the analysis is completed by creating a static general step, where the temperature-time history generated from the heat transfer step is given as an input. In the sequentially coupled analysis, the pure heat transfer step is done without setting any mechanical boundary conditions or constraints in the model whereas; appropriate boundary conditions are applied in the second stage, i.e., the thermal stress analysis.

The initial temperature of the spur gear is 850 °C. Also, the interaction surface is assigned with an average surface film coefficient of 1950 $W/m^2 \cdot K$ [19] with a sink temperature of 25 °C in both methods. The analysis is run for 30 s until the gear cools to 25 °C.

In this analysis, a pathway is created to observe the behavior of the estimates along that track and is highlighted in red in Fig. 2.2 starting from node 39 and ending at node 40. The point of origin for the quarter gear is defined by the global coordinate system, i.e., the intersection of the X-, Y-, and Z-axes in Fig. 2.2. The XY-plane contains the origin and in that sense, node 39 is the vertex of the middle tooth of the quarter gear in the XY-plane. Node 44 is just located vertically above node 39 in a plane parallel to the XY-plane at a height of 6.35 mm from

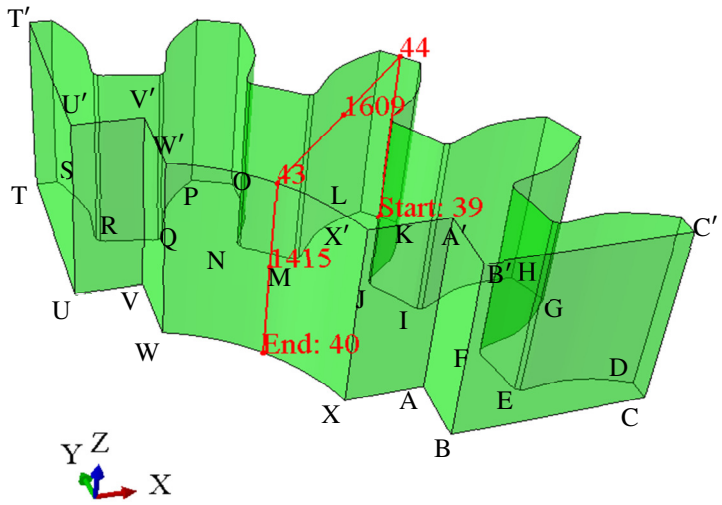


Figure 2.2: Quarter of a spur gear with the pathway of analysis

node 39. Node 43 is in the same plane of node 44 located at the top inner arc of the quarter gear at a radial distance of 5.9 mm from node 44. Node 40 is just located vertically below the node 43 in the XY-plane. Node 1609 and node 1415 are located almost midway of the paths 44→43 and 43→40, respectively. The global coordinates of all the nodes in Fig. 2.2 are shown in Table 2.3.

Table 2.3: Global coordinates of the nodes in Fig. 2.2

| Node label | X coordinate, mm | Y coordinate, mm | Z coordinate, mm |
|---|---|---|---|
| 39 | 10.11 | 10.11 | 0 |
| 40 | 4.53 | 4.53 | 0 |
| 43 | 4.53 | 4.53 | 6.35 |
| 44 | 10.11 | 10.11 | 6.35 |
| 1415 | 4.53 | 4.53 | 3.33 |
| 1609 | 7.38 | 7.38 | 6.35 |

## 2.6 Boundary Conditions

Table 2.4 shows the necessary boundary conditions relevant to the boundaries as described in Fig. 2.2 where $U$ is the displacement and $UR$ is the rotation with 1, 2, and 3 as the

subscripts representing the X-, Y-, and Z-axes, respectively. The first boundary condition indicates that the inner curved surface of the spur gear including the areas of the key slots does not have any displacement along the X- or Y-directions i.e., along the radial direction. The only direction to which the deformation is allowed is the Z-axis. This is because; after quenching, the gear would have a tendency to shrink in all directions and if the inner curved surface of the quarter gear including the key slot areas is not allowed to move radially, then the gear can shrink only along the vertical direction.

Table 2.4: Boundary conditions for the quarter spur gear

| Surfaces | Degrees of freedom |
|---|---|
| UVWXABB′A′X′W′V′U′ | $U_1=U_2=UR_3=0$ |
| BCC′B′ | $U_2=UR_1=UR_3=0$ |
| UTT′U′ | $U_1=UR_2=UR_3=0$ |
| CDEFGHIJKLMNOPQRSTUVWXAB | $U_3=UR_1=UR_2=0$ |

The second and the third boundary conditions indicate that the vertical planes $BCC'B'$ and $UTT'U'$ remain in the respective vertical planes while quenching. For plane $BCC'B'$, deformation is allowed along X- or Z-axis and rotation is constrained to occur only in the XZ-plane (no rotation with respect to X- or Z-axis). For plane $UTT'U'$, deformation is allowed along Y- or Z-axis and rotation is restricted to occur only in the YZ-plane (no rotation with respect to Y- or Z-axis). These boundary conditions are set accordingly because both planes are the planes of symmetry of the spur gear.

Finally, the fourth boundary condition describes that the bottom XY-plane remain in the same plane and is not displaced. No rotation of this plane occurs with respect to the Z-axis. This condition is set because the XY-plane is also one of the planes of symmetry.

## 2.7 Mesh Generation

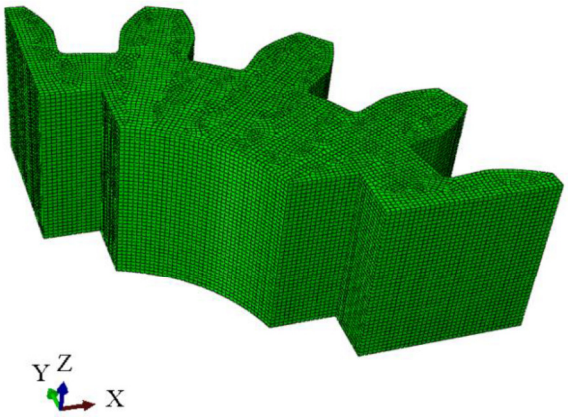


Figure 2.3: Mesh of the quarter gear with element size of 0.16 mm

The quarter gear is partitioned into eight segments to ensure a good, uniform mesh and to avoid deformation of mesh elements. Fig. 2.3 represents the meshed gear with the finest element size of 0.16 mm. After meshing, the quarter gear has 156,640 elements and 169,412 nodes. Structural meshing is preferred to avoid any distortion of the mesh elements. For fully coupled analysis, C3D8RT (eight-node thermally coupled brick, tri-linear displacement and temperature, reduced integration) elements are used. For sequentially coupled analysis, DC3D8 (eight-node linear heat transfer brick) elements are used for heat transfer and C3D8R (eight-node, linear brick, reduced integration) elements are used to calculate the 3-D stress throughout the spur gear.

# 3. Dynamic Quenching Analysis of a Steel Tube

## 3.1 Scope of Quenching of a Steel Tube

Steel tubes with various wall thicknesses are most commonly used as machine components in a mechanism as connecting, rotating, or, rolling components, generator shafts, pressure vessels, etc. They have to withstand high dynamic torsional and compressive stresses and should have enhanced toughness and fatigue resistance for better performance and longer life. Hence, steel tubes need to be quenched for obtaining improved properties. Since steel tubes are the basic forms of many mechanical components, it is important to observe the transient temperature distribution throughout the steel tube after quenching and the distribution of the stress and deformation along radial and axial pathways of the tube. Therefore, in this Chapter, a 3-D FSI model is developed consisting of the solid steel tube and the liquid quenchant to evaluate at first the thermal interaction between the tube and the quenchant. After that, the thermal stress is calculated based on the previous thermal interaction. The time-varying temperature distributions for three different nodes are investigated. Also, the residual stress and deformation at a particular point and along the axial and radial directions of the tube after quenching are studied. The cooling rates of all the three liquids are compared with each other and the critical regions in the tube are identified after quenching.

## 3.2 Description of the Steel Tube

The steel tube has the inner and the outer radii of 1.2 mm and 2.5 mm, respectively, with a height of 9.0 mm and is considered homogeneous. All the standard dimensions are chosen from precision bushing catalog [34]. A relatively smaller tube is chosen to save computational time and to make more accurate analysis.

## 3.3 Properties of the Steel Tube

Properties of the steel tube are given in Table 3.1 [18]. The tube is assumed to be made of an elastic, perfectly plastic steel with a temperature dependent yield stress as mentioned in Chapter 2 by Eqs. 1 and 2. All the properties of the steel tube are considered isotropic.

Table 3.1: Properties of the steel tube

| | |
|---|---|
| Density, $kg/m^3$ | 7830 |
| Young's modulus, Pa | 206.8e9 |
| Poisson's ratio | 0.3 |
| Thermal conductivity, W/m·K | 58.8 |
| Specific heat, J/kg·K | 600 |
| Coefficient of thermal expansion, $K^{-1}$ | 0.0000135 |

## 3.4 Properties of the Liquid Quenchants

Three different liquid quenchants are used in this analysis namely water [35], 20% w/w brine aqueous solution [36], and 10% w/w PG aqueous solution [37]. The properties of the liquid quenchants at 25 °C are given in Table 3.2. The solution concentration unit w/w for both brine and PG indicates the ratio of the mass of the solute to that of the solvent in a solution.

Table 3.2: Properties of the liquid quenchants at 25 °C

| Property | Water | 20% w/w brine aqueous solution | 10% w/w PG aqueous solution |
|---|---|---|---|
| Density, $kg/m^3$ | 1000 | 1133 | 1004 |
| Viscosity, Pa·s | 0.891e–3 | 1.26e–3 | 1.2e–3 |
| Thermal conductivity, W/m·K | 0.61 | 0.494 | 0.565 |
| Specific heat, J/kg·K | 4200 | 3430 | 4200 |

## 3.5 The Fluid-Structure Interaction Model

The 3-D FSI model consists of the cylindrical steel tube as the solid FE model and the rectangular liquid quenchant domain as the CFD model, for investigating the residual stress and deformation in the tube by using the commercially available FE software, Abaqus 6.12 [33]. The dynamic analysis is run in a transient mode by a sequentially coupled analysis. The sequentially coupled analysis, as described in Chapter 2, consists of two steps; the pure transient heat transfer analysis between the tube and the quenchant at first and then the thermal stress analysis of the tube. In the first step, the heat transfer analysis is carried out by coupling the FE model with the CFD model to generate the temperature-time history as an output until the tube reaches the sink temperature. It is a multi-physics coupling such that the fluid flows over the tube and takes away the heat to cool it. Once the temperature-time history in the heat transfer step is obtained, it is used as an input in the second step where a static FE model is used to estimate the thermal stress and deformation in the tube. The initial temperature of the tube and all the liquid quenchants are 850 °C [19] and 25 °C, respectively. The sink temperature for the tube is set as 25 °C.

### 3.5.1 General Mathematical Formulation for the CFD Model

The mathematical formulation for the CFD model predicts the primitive variables of density, velocity, pressure, and temperature within the fluid domain which requires the solution of the continuity, momentum (Navier-Stokes equations), and the energy equations. The general mathematical formulation of the above conservation equations starting from vector form with appropriate boundary conditions and initial conditions are discussed in the following sections. Later, depending on our specific physical flow model, the corresponding boundary conditions and initial conditions are defined in section 3.5.4.

#### *3.5.1.1 General Assumptions*

1. The fluid flow is assumed to be incompressible.
2. The flow is laminar and viscous.
3. The working fluid behaves like a Newtonian fluid with stokes assumptions.
4. The physical properties of the fluids are assumed to be constant.

#### *3.5.1.2 Conservation of Mass (Continuity Equation)*

The general continuity equation in vector form for any fluid,

$$\frac{\partial \rho_f}{\partial t} + \boldsymbol{\nabla}.\left(\rho_f \boldsymbol{V}\right) = 0 \tag{3.1}$$

where, $\boldsymbol{V}$ indicates the velocity vector, $\rho_f$ is the density of the fluid, and $t$ represents time.

From assumption 1, for incompressible flow,

$$\frac{\partial \rho_f}{\partial t} = 0 \tag{3.2}$$

Using the above relation in Eq. 3.1 and by assumption 4, the continuity equation becomes,

$$\boldsymbol{\nabla}.\boldsymbol{V} = \mathbf{0} \tag{3.3}$$

From Eq. 3.3, the modified continuity equation can be written in scalar form,

$$\frac{\partial u}{\partial x} + \frac{\partial v}{\partial y} + \frac{\partial w}{\partial z} = 0 \tag{3.4}$$

where, $u, v,$ and $w$ indicates the velocity components of the fluid in $x, y,$ and $z$ directions, respectively. Eq. 3.3 represents the most general form of the continuity equation for incompressible flow.

#### *3.5.1.3 Conservation of Momentum (Navier-Stokes Equations)*

The general momentum equation in vector form for an incompressible flow with constant properties (assumptions 1 and 4),

$$\rho_f \left(\frac{\partial \boldsymbol{V}}{\partial t} + \boldsymbol{V}.\boldsymbol{\nabla V}\right) = -\boldsymbol{\nabla} p + \mu \nabla^2 \boldsymbol{V} + \rho_f \boldsymbol{g} \tag{3.5}$$

where, $p$ is the thermodynamic pressure, $\mu$ is the dynamic viscosity of fluid, and $\boldsymbol{g}$ is the acceleration vector due to gravity.

The corresponding $x, y,$ and $z$ momentum equations in scalar form are as follows:

$$\rho_f \left(\frac{\partial u}{\partial t} + u\frac{\partial u}{\partial x} + v\frac{\partial u}{\partial y} + w\frac{\partial u}{\partial z}\right) = -\rho_f g_x - \frac{\partial p}{\partial x} + \mu\left(\frac{\partial^2 u}{\partial x^2} + \frac{\partial^2 u}{\partial y^2} + \frac{\partial^2 u}{\partial z^2}\right) \tag{3.6}$$

$$\rho_f \left(\frac{\partial v}{\partial t} + u\frac{\partial v}{\partial x} + v\frac{\partial v}{\partial y} + w\frac{\partial v}{\partial z}\right) = -\rho_f g_y - \frac{\partial p}{\partial y} + \mu\left(\frac{\partial^2 v}{\partial x^2} + \frac{\partial^2 v}{\partial y^2} + \frac{\partial^2 v}{\partial z^2}\right) \tag{3.7}$$

$$\rho_f \left(\frac{\partial w}{\partial t} + u\frac{\partial w}{\partial x} + v\frac{\partial w}{\partial y} + w\frac{\partial w}{\partial z}\right) = -\rho_f g_z - \frac{\partial p}{\partial z} + \mu\left(\frac{\partial^2 w}{\partial x^2} + \frac{\partial^2 w}{\partial y^2} + \frac{\partial^2 w}{\partial z^2}\right) \tag{3.8}$$

#### *3.5.1.4 Conservation of Energy (Energy Equation)*

The vector form of the energy equation for an incompressible flow the fluid domain can be described as,

$$\rho_f C_{pf} \frac{DT_f}{Dt} = \beta T_f \frac{Dp}{Dt} - \boldsymbol{\nabla}.\boldsymbol{q} + \Phi \tag{3.9}$$

where,

$C_{pf}$ is the specific heat of the fluid at constant pressure

$T_f$ is the variable temperature within the fluid body

$\beta$ is the volumetric thermal expansion coefficient

$\boldsymbol{q}$ is the heat flux vector due to conduction, and

$\Phi$ is the dissipation function defined as,

$$\Phi = \tau'_{ij} \frac{\partial v_i}{\partial x_j} \tag{3.10}$$

where, $\tau'_{ij}$ is the shear stress and $\frac{\partial v_i}{\partial x_j}$ indicates the velocity gradient in the fluid domain.

If the velocity $V$ becomes smaller and heat transfer remains important, the fluid kinetic energy term containing $V^2$ will eventually become much smaller than the enthalpy change $C_{pf}\Delta T$. Since both $\frac{Dp}{Dt}$ and $\Phi$ are of order $V^2$, we can neglect them and eventually Eq. 3.9 becomes,

$$\rho_f C_{pf} \frac{DT_f}{Dt} = -\boldsymbol{\nabla}.\boldsymbol{q} \tag{3.11}$$

Neglecting radiative heat transfer, $\boldsymbol{q}$ can be calculated from Fourier's law of heat conduction,

$$\boldsymbol{q} = -k_f \boldsymbol{\nabla} T_f \tag{3.12}$$

where, $k_f$ is the thermal conductivity of the fluid.

Substituting this value of $\boldsymbol{q}$ into Eq. 3.11, we get,

$$\rho_f C_{pf} \frac{DT_f}{Dt} = -\boldsymbol{\nabla}.\left(-k_f \boldsymbol{\nabla} T_f\right) \tag{3.13}$$

By assumption 4, $k_f$ is constant and can be drawn out from the divergence operator to give,

$$\rho_f C_{pf}\left(\frac{\partial T_f}{\partial t} + \boldsymbol{V}.\boldsymbol{\nabla} T_f\right) = k_f \nabla^2 T_f \tag{3.14}$$

Eq. 3.14 can be expanded in scalar form in terms of the temperature gradients in $x, y,$ and $z$ directions as,

$$\rho_f C_{pf}\left(\frac{\partial T_f}{\partial t} + u\frac{\partial T_f}{\partial x} + v\frac{\partial T_f}{\partial y} + w\frac{\partial T_f}{\partial z}\right) = k\left(\frac{\partial^2 T_f}{\partial x^2} + \frac{\partial^2 T_f}{\partial y^2} + \frac{\partial^2 T_f}{\partial z^2}\right) \tag{3.15}$$

#### *3.5.1.5 Boundary and Initial Conditions*

The boundary conditions for a viscous, heat conducting flow involve three most common type of boundaries described in Fig. 3.1,

1. The fluid-solid interface
2. The fluid-fluid interface
3. The inlet or exit section of the fluid domain

**1. The fluid-solid interface:** At the fluid-solid interface, there must be no slip of fluid due to viscosity effect. So, the no slip boundary conditions are,

$$\boldsymbol{V}_f = \boldsymbol{V}_s \qquad \text{or} \qquad \boldsymbol{V}_f = \boldsymbol{V}_w \tag{3.16}$$

where, the subscripts $f, s,$ and $w$ stands for fluid, solid, and wall, respectively.
When, the fluid conducts heat from the wall, then, either there will be no temperature jump (when the wall temperature is known or can be found from other relationships),

$$T_f = T_s \qquad \text{or} \qquad T_f = T_w \tag{3.17}$$

or, equality of the heat flux (when the solid heat flux is known) from solid to fluid,

$$k_f \frac{\partial T_f}{\partial n} = q \tag{3.18}$$

where, $n$ indicates the direction normal to the fluid surface adjacent to the wall.

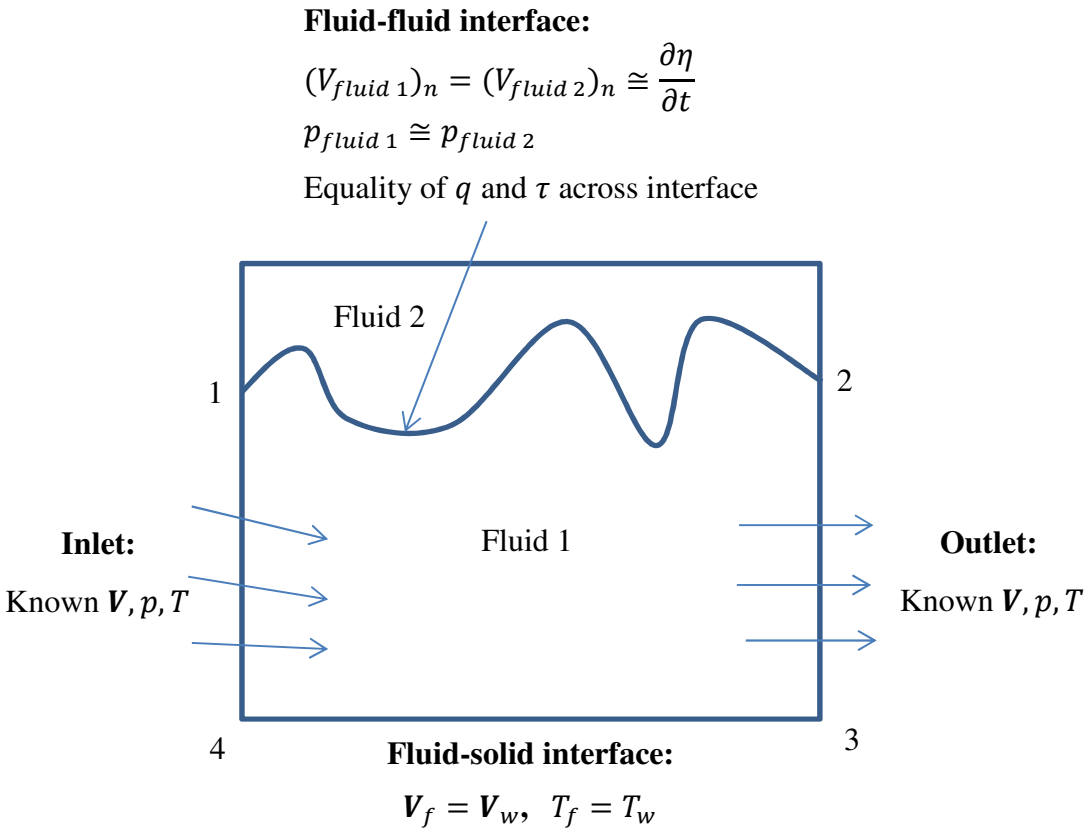


Figure 3.1: Typical boundary conditions in a viscous heat-conducting fluid flow analysis

**2. The fluid-fluid interface:** At the interface between two fluids, there must be kinematic equivalence, i.e., there must be equality of the normal velocity across the fluid-fluid interface so that no holes appear between them, which is also known as the kinematic boundary condition. If we denote the fluid 1 and fluid 2 interface 1-2 in Fig. 3.1 by $\eta$, then the boundary condition at the interface 1-2 would be,

$$(V_{fluid\,1})_n = (V_{fluid\,2})_n \cong \frac{\partial \eta}{\partial t} \tag{3.19}$$

There must be mechanical equilibrium across the interface. The viscous shear stresses must balance:

$$\left(\tau_{fluid\,1}\right)_{interface} = \left(\tau_{fluid\,2}\right)_{interface} \tag{3.20}$$

Neglecting the viscous normal stresses, the pressure at the interface except for surface tension effects (negligible in most cases) must be balanced as,

$$p_{fluid\,1} \approx p_{fluid\,2} \tag{3.21}$$

Finally the heat transfer must be same on both sides of the interface, since no heat can be stored in the infinitesimally thin interface and neglecting radiation which is equivalent to

$$\left(q_{fluid\,1}\right)_n = \left(q_{fluid\,2}\right)_n \tag{3.22}$$

**3. The inlet or exit section:** At any inlet or outlet section of the flow, the complete distribution of the velocity, pressure, and temperature must be known every point on the boundary which sets the boundary conditions as; known $V, p,$ and $T$ at inlet and exit.

If the flow is unsteady, there must be an initial condition or initial spatial distribution known for the primitive variables. Hence, for the most general case, the initial condition is written as; known $V, p,$ and $T$ at $t = 0$, where $V, p,$ and $T$ are different functions of $x, y,$ and $z$.

### 3.5.2 Physical Domain

Figures 3.2 and 3.3 show the computational fluid domain for the liquid quenchant and the steel tube, respectively. The point of origin for both the fluid and the solid domain is the intersection of the X-, Y-, and Z-axes which lies in the same XY-plane common for both domains as shown in Figs. 3.2 and 3.3. The fluid domain in Fig. 3.2 has the length of 25 mm in

the X-direction, the width of 20 mm in the Y-direction, and the height of 15 mm in the Z-direction. The solid domain in Fig. 3.3 has the same dimensions as described before for the steel tube in the property section. The surface of the tube in the XY-plane is will be noted asthe bottom surface of the tube.

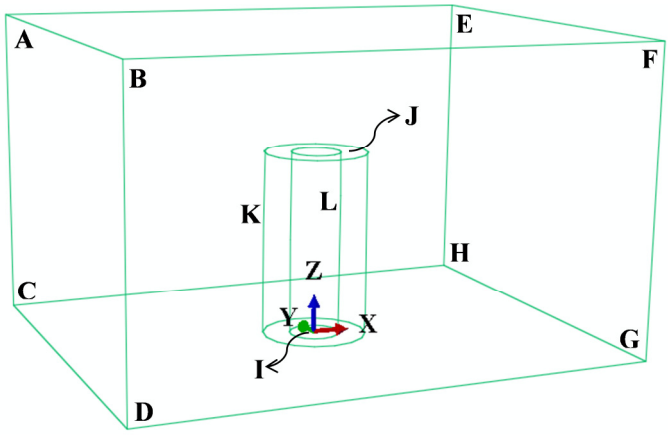


Figure 3.2: Computational domain for the liquid quenchant

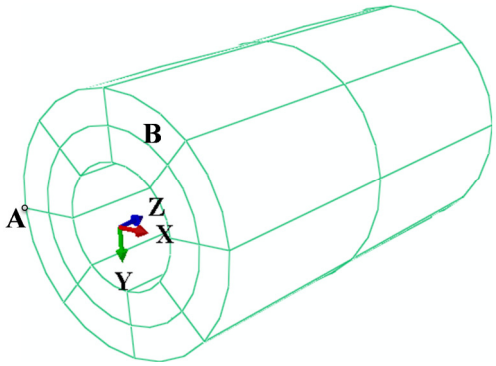


Figure 3.3: Computational domain for the steel tube

Figure 3.4 describes the longitudinal cross-section of the steel tube about the YZ-plane where an axial path AB from node 52 to node 25 and a radial path CD from node 68 to node 27, are created to see the distribution of the stress and deformation along the normalized distance. The normalized distance is a dimensionless distance defined as the ratio of any distance from the start of the path to the length of the path. To monitor the time-varying temperature, two nodes J

and K are randomly chosen in the tube. Node J is located on the top surface of the tube in the upstream direction of flow on the periphery of a circle having a radius of 1.85 mm along negative X-axis. Node K is located in the longitudinal cross-section FGHI of the tube near the vicinity of the bottom surface. Node E is the intersection point as well as the midpoint of both paths AB and CD. Table 3.3 enumerates the coordinates of all the nodes described in Fig. 3.4.

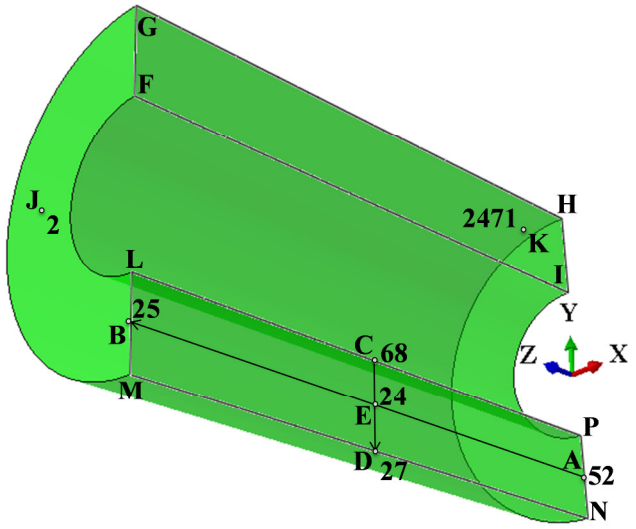


Figure 3.4: Half of the tube with locations of paths (AB and CD) and nodes (2, 24, 25, 27, 52, 68, and 2471) of analysis

Table 3.3: Global coordinates of the nodes in Fig. 3.4

| Node label | X-coordinate, mm | Y-coordinate, mm | Z-coordinate, mm |
|---|---|---|---|
| 2 | -1.85 | 0 | 9 |
| 24 | 0 | -1.85 | 4.5 |
| 25 | 0 | -1.85 | 9 |
| 27 | 0 | -2.5 | 4.5 |
| 52 | 0 | -1.85 | 0 |
| 68 | 0 | -1.2 | 4.5 |
| 2471 | 0 | 2.067 | 0.783 |

### 3.5.3 Interaction

The interaction surface is the common, shared surface between the tube and the quenchant through which heat transfer occurs. The whole surface area of the tube except the bottom surface is the interaction surface also known as fluid-structure co-simulation boundary. The interaction surface for the tube can be visualized easily from Fig. 3.2 which is the union of the top surface J, the outer surface K, and the inner surface L of the tube inside the fluid domain.

### 3.5.4 Boundary and Initial Conditions

#### *3.5.4.1 For CFD Model*

Table 3.4: Boundary conditions for fluid domain

| | | Boundary conditions | | | | |
|---|---|---|---|---|---|---|
| | | Velocity, m/s | | | | |
| Name | Surfaces | $u$ | $v$ | $w$ | Pressure, Pa | Temperature, ºC |
| In-flow | ABDC | 1 | 0 | 0 | - | - |
| Top-flow | ABFE | 1 | 0 | 0 | - | - |
| Side-flow | BFGD | 1 | 0 | 0 | - | - |
| Side-flow | AEHC | 1 | 0 | 0 | - | - |
| Out-flow | EFGH | - | - | - | 0 | - |
| No-slip | CDGH+I+J+K+L | 0 | 0 | 0 | - | - |
| No-temperature jump | CDGH+I+J+K+L | 0 | 0 | 0 | - | $T_f = T_{solidsurface}$ |

The boundary conditions for the CFD model (the fluid domain) are shown in Table 3.4 with reference to Fig 3.2. For the fluid domain, the boundary conditions are specified in terms of velocity, pressure, or temperature. As mentioned in the mathematical formulation; $u, v,$ and $w$ indicate the velocity components along X-, Y-, and Z-directions (upper case notations according to Fig. 3.2), respectively. The velocities on the top and the side boundaries of the fluid domain

are considered the same as that for the in-flow. This is because; the fluid domain is small enough to justify the consideration of parallel flow. It is a reasonable assumption to set zero velocity in Y- and Z-directions. The no-slip boundary condition contains surface CDGH and surface I in Fig. 3.2 including the interaction surface. The no-temperature jump boundary condition indicates that at the hot outer and inner surfaces of the steel tube, the adjacent fluid layers in touch must have the same temperature of the corresponding surfaces.

The heat from the hot solid surface of the steel tube to the liquid is transferred in two steps. At first, the heat will transfer from the hot tube surface to the touching adjacent but very thin stagnant layer of liquid mainly by conduction through the thickness of the layer and also by convection which is negligible. In the next step, the heat from the thin liquid layer will negligibly be conducted to the surrounding fluid buy significantly by convection. Mathematically, we can express this by,

$$(Q_{conduction} + Q_{convection})_{thin\ layer} = (Q_{conduction} + Q_{convection})_{surrounding\ fluid}$$

$$(Q_{conduction})_{thin\ layer} \cong (Q_{convection})_{surrounding\ fluid}$$

$$-\left(k_f A_x \frac{dT}{dx} + k_f A_y \frac{dT}{dy} + k_f A_z \frac{dT}{dz}\right) \cong hA_{layer}\left(T_f - T_{freestream}\right) \tag{3.23}$$

where,

$Q$ is the heat transferred either by conduction or convection

$A_x$, $A_y$, and $A_z$ indicate the heat conduction areas in the thin liquid layer normal to the $x, y,$ and $z$ directions, respectively

$h$ is the average heat transfer coefficient

$A_{layer}$ is the outer area of the thin fluid layer separating the bulk fluid from the tube wall

$\frac{dT}{dx}$, $\frac{dT}{dy}$, and $\frac{dT}{dz}$ indicate the temperature gradients in the thin liquid layer in $x, y$, and $z$ direction respectively and the temperature derivative is defined as,

$$\frac{dT}{dn} = \lim_{\Delta n \to 0} \frac{T_{n+\Delta n} - T_n}{\Delta n} = \lim_{\Delta n \to 0} \frac{T_{solidsurface} - T_f}{\Delta n}$$

where, $n$ indicates either $x, y$, or $z$ direction.

Since we are not considering a steady flow analysis, the initial conditions must be defined at the start of our analysis for the CFD model. The initial conditions are stated below:

**1. Initial condition for velocity:** The free stream velocity of fluid applied at the left boundary of the fluid domain in Fig. 3.2 represents the initial velocity condition as; $u = 1\ m/s$, $v = 0$, and $z = 0$ at $t = 0$.

**2. Initial condition for temperature:** It is the temperature of the fluid in the free stream location applied at the left boundary of the CFD model in Fig. 3.2 and is prescribed as $T_f = 25\ ℃$ at $t = 0$.

***3.5.4.2 For Solid Model***

For the solid domain, the boundary conditions are specified in terms of the displacement and the rotation with reference to Fig. 3.3. In Table 3.5, $s$ and $\theta$ indicate the displacement and the rotation of the tube, respectively, with the corresponding subscripts. For the solid domain in Fig. 3.3, surface B is the whole bottom surface of the tube which always remains in XY-plane during quenching for which $s_z$ is zero. The fixed point A is located on the bottom surface of the tube in the outermost edge along negative X-axis in the upstream direction of flow and all kinds of

displacements and rotations are zero on that point. The initial condition for the solid tube in terms of temperature is set as; $T_{wholetube} = T_{solidsurface} = 850$ °C at $t = 0$.

Table 3.5: Boundary conditions for solid domain

| Name | Surface or point | Boundary conditions | | | | | |
|---|---|---|---|---|---|---|---|
| | | Displacement, m | | | Rotation, degrees | | |
| | | $s_x$ | $s_y$ | $s_z$ | $\theta_x$ | $\theta_y$ | $\theta_z$ |
| Bottom surface | B | - | - | 0 | - | - | - |
| Fixed point | A | 0 | 0 | 0 | 0 | 0 | 0 |

### 3.5.5 Mesh Generation

#### *3.5.5.1 For CFD Model*

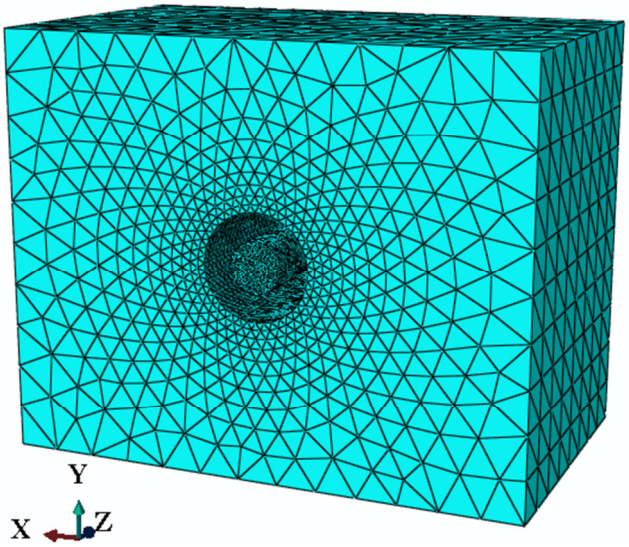


Figure 3.5: The fluid domain after meshing

Figure 3.5 shows the meshed fluid domain with the finest element size of 2 mm. A high density mesh is created near the outer and the inner surface of the cavity within the fluid domain by considering 40 elements on the outer periphery and 35 elements on the inner periphery of the

cavity. The rectangular fluid domain in the CFD model is meshed by FC3D4 (four-node, linear, fluid-tetrahedron), 3-D stress elements.

#### *3.5.5.2 For Solid Model*

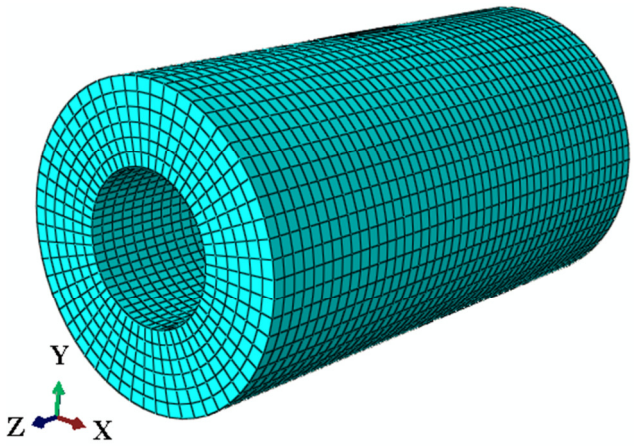


Figure 3.6: The steel tube after meshing

Figure 3.4 represents the meshed FE model of the steel tube with the finest element size of 0.2 mm. For more accuracy, structured meshing is considered. The tube is symmetrically partitioned by eight axial planes and by one radial plane through the center of the tube axis. After meshing, the tube has 15,456 elements and 18,424 nodes which are kept same for both heat transfer and thermal stress analyses. In this sequentially coupled analysis, DC3D8 (eight-node linear heat transfer brick) elements are used for the heat transfer step and after that, C3D8R (eight-node, linear brick, reduced integration) elements are used to calculate the 3-D stress. The solid FE model developed in Abaqus/Standard and the CFD model developed in Abaqus/CFD are coupled to run the FSI analysis by creating the co-execution jobs for both models [33].

# 4. Results and Discussions

## 4.1 Static Quenching Analysis of a Spur Gear

### 4.1.1 Model Validation

For validating the FE model, the residual stress computed by Landau et al. [18] for an infinite plate with one-dimensional (1-D) heat transfer is compared with that of the developed FE model. Landau et al. [18] showed the residual stress distribution after quenching of an infinite steel plate of thickness 36 inch only in the thickness direction. An axisymmetric analysis from center of the plate up to thickness of 18 inch was carried out. The boundary conditions of the axisymmetric model involved no movements of the X- and Y-axes, in vertical and horizontal directions, respectively. The FE model computes the 1-D residual stress as reported in Ref. [18] by both fully and sequentially coupled analyses. The maximum variation of the stress computed by two models (Ref. [18] and developed FE model) is 8%. As the FE model for 1-D quenching workes well, the current 3-D model of the gear is investigated for further analysis.

In this analysis of the quarter gear in Chapter 2, the estimates are in an excellent agreement with both fully and sequentially coupled analysis for the finest mesh size of 0.16 mm. A comparison of the results from both methods is shown in Table 6.

Table 4.1: Comparison of fully coupled and sequentially coupled analysis

| Fully coupled analysis | | | | Sequentially coupled analysis | | | |
|---|---|---|---|---|---|---|---|
| von-Mises stress, MPa | | Deformation, mm | | von-Mises stress, MPa | | Deformation, mm | |
| Max. | Min. | Max. | Min. | Max. | Min. | Max. | Min. |
| 248 | 0.78 | 0.128 | 0 | 248 | 0.76 | 0.128 | 0 |

### 4.1.2 Convergence Study and the Cooling Curve

Figure 4.1 shows the variation of stresses at different nodes with degrees of freedom (DOF) for different meshes. 14 different mesh elements of size 2.0, 1.8, 1.5, 1.2, 1.0, 0.8, 0.5, 0.4, 0.3, 0.25, 0.22, 0.2, 0.18, and 0.16 mm are used for the simulation until the convergence or mesh independence condition is obtained. As the DOFs increase, stresses fluctuate initially and after that become flattened indicating that the solution has already become mesh independent. The mesh independence study is done for three different nodes as shown in Fig. 4.1.

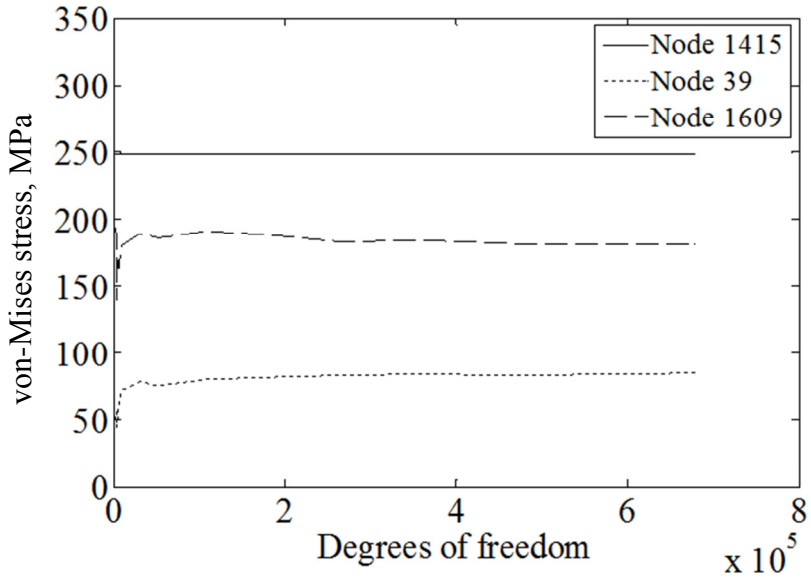


Figure 4.1: Variations of the von-Mises stresses at different nodes with degrees of freedom

Figure 4.2 gives the temperature-time history for five nodes located in surface ABCD, the middle vertical plane in the quarter gear in Fig. 2.2. Nodes 39, 44, and 1609 are on the boundary while nodes 14983 and 15979 are internal ones. The temperature of each node decreases with time in an exponential way as the gear cools from 850 °C to 25 °C. The cooling curves for nodes 14983 (X=5.43712 mm, Y=5.43789 mm, and Z=1.11125 mm) and 15979 (X=6.80506 mm, Y=6.80603 mm, and Z=4.445 mm) are the top ones indicating lower cooling rates compared to

those of nodes 39, 44, and 1609 as they did not come directly to the exposure of the cooling environment. The time-varying temperature distribution for each node follows similar trend up to 15 s and are merged after that. It is clear from the cooling curve that the cooling rate decreases as the temperature difference between the gear and the surrounding decreases. The slopes of the cooling curves indicate respective cooling rates almost zero after 15 s for all of the nodes.

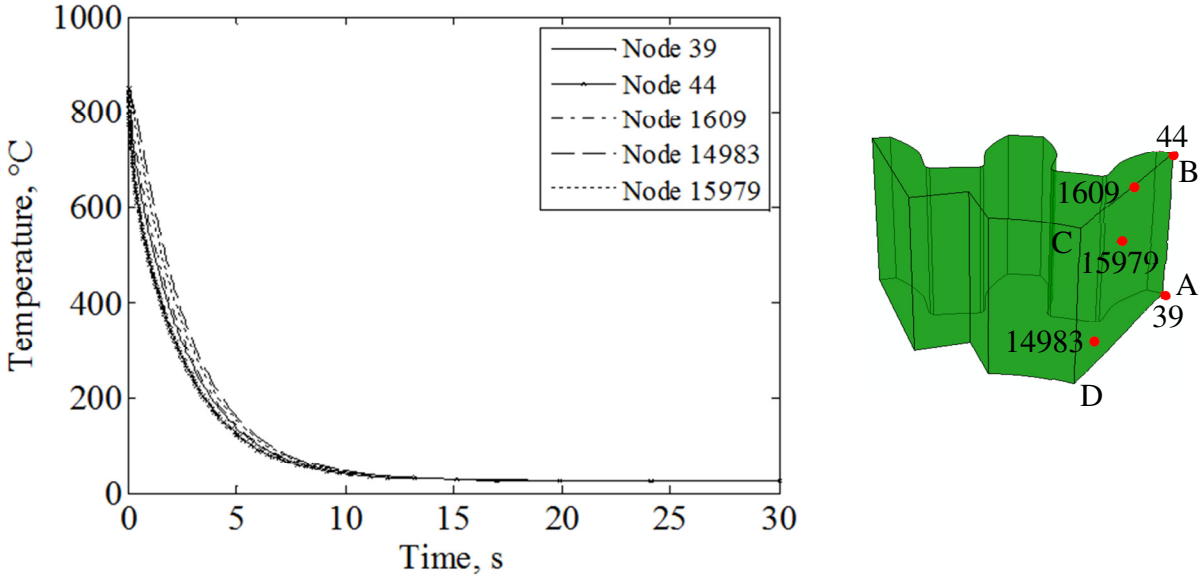


Figure 4.2: Variations of the nodal temperatures with time

### 4.1.3 Stress and Deformation Analysis

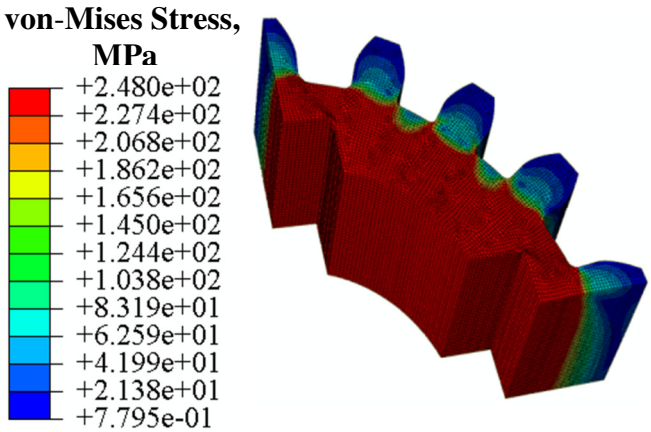


Figure 4.3: Distribution of the von-Mises stress in the quarter gear

From Fig. 4.3, the highest stress developed in the gear is 248 MPa that covers the region from the inner bore edge up to the tooth root and reduces from the tooth root to the tooth tip of the gear radially inwards. The stress also varies through the tooth along the gear thickness. From Fig. 4.4, the deformation varies from the bottom plane to the top plane of the gear and increases from the inner bore edge to the tooth tip with a peak value of 0.128 mm.

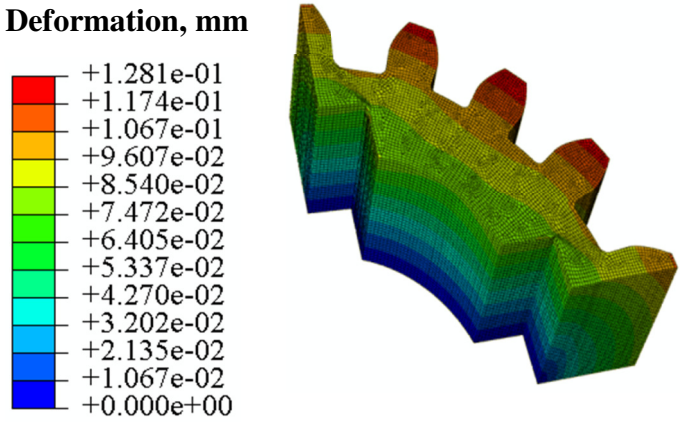


Figure 4.4: Distribution of the deformation in the quarter gear

### 4.1.4 Time-varying Nodal Stress and Deformation

The behavior of the time-varying stresses at nodes 39, 1415, and 1609 are plotted in Fig. 4.5 which depicts that after around 7 s, all the curves get flattened, although they have some initial stress fluctuations. Nodes 39 and 1415 have the leveled stress of 84 MPa and 284 MPa, respectively. The stress for node 1609 is 181.4 MPa for most of the time. Node 1415 has higher stress than that of node 1609, as the former is located on a curved surface. The behavior of the time-varying deformations at nodes 39, 1415, and 1609 are visible in Fig. 4.6 where all the curves show a sharp increase of deformation within 5 s. Compared to Fig. 4.5, node 39 has no fluctuation in deformation as seen from Fig. 4.6. Also, from Fig. 4.6, the deformations of nodes 39 and 1609 are very close unlike respective stresses given by Fig. 4.5.

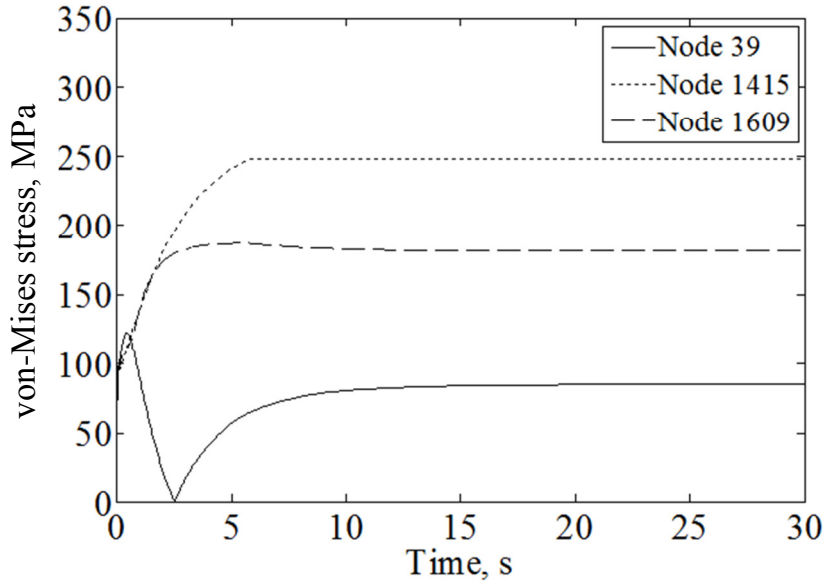


Figure 4.5: Variations of the von-Mises stresses at different nodes with time

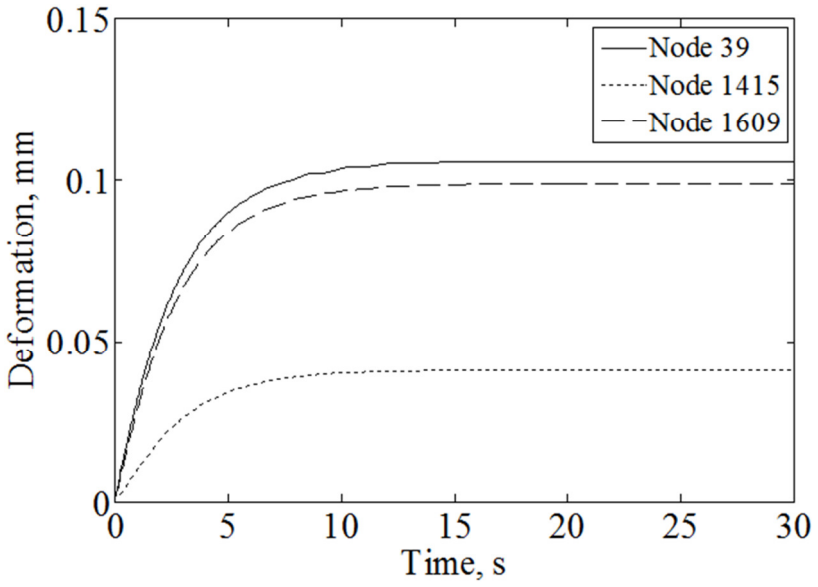


Figure 4.6: Variations of the deformations at different nodes with time

### 4.1.5 Path-wise Stress and Deformation

The variation of the von-Mises stress with normalized distance along the pathway from node 39 to node 40 is given in Fig. 4.7 where the normalized distance is calculated by dividing the distance of any node from node 39 by the total linear distance between node 39 and node 40.

Fig. 4.7 gives a fluctuating pattern of stress along the path from node 39 to node 40 (pathway 39→40). As node 39 is more constrained than the top nodes, it shows the highest stress of 84 MPa among all the nodes in the pathway 39→44 and starts decreasing after that until it reaches node 44 at a normalized distance of 0.3 with 2 MPa stress. For pathway 44→43, the stress level increases, then decreases, and again increases ending up to 248 MPa at normalized distance 0.53 and continues the trend up to node 40. The overall stress fluctuation is due to the unequal movement of the inner nodes not very free to move compared to the outer ones.

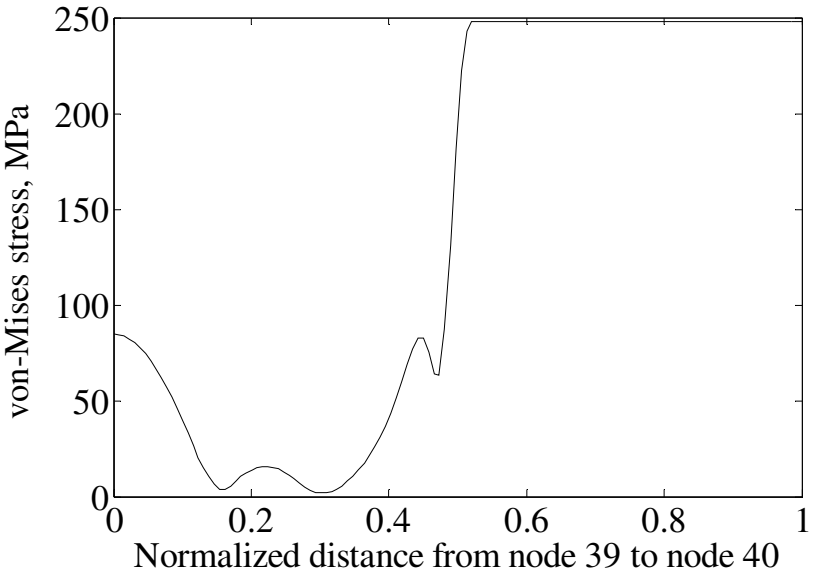


Figure 4.7: Variation of the von-Mises stress along the path 39→40

Comparing Figs. 4(b) and 5(b), a trend of decreasing stress in Fig. 4(a) is counter parted by increasing deformation in Fig. 5(b) within node path 39→44. The opposite behavior is seen for node path 44→43. The highest stress developed in the gear is the plastic yield stress limit of the gear material; consequently, a proportional stress-strain relationship within the elastic limit does not work. For node path 39→44, the upper nodes are freer to move compared to node 39 and they experience more deformation. Due to the constraint, the bottommost node 39 shows the

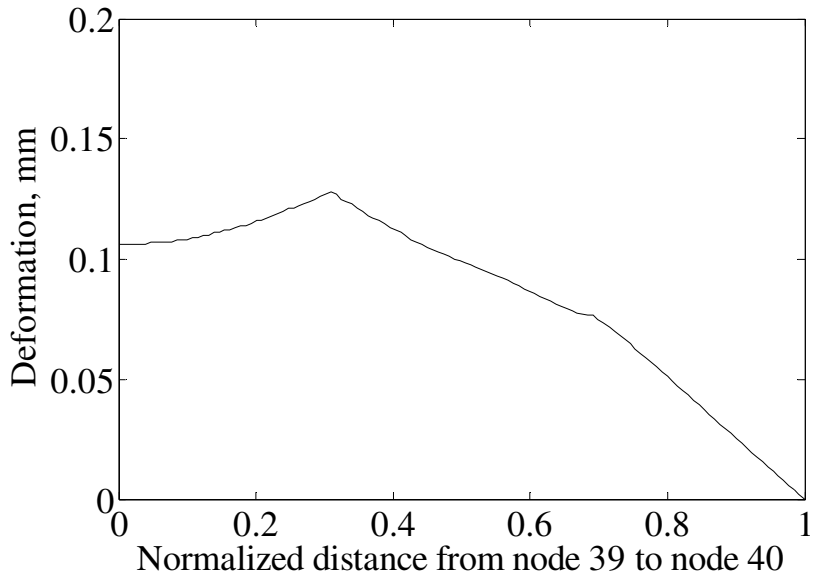


Figure 4.8: Variation of the deformation along the path 39→40

least deformation but higher stress up to node 44 when considered the pathway 39→44. For pathway 44→43, the nodes at the outer edge of the quarter gear have more freedom to move then the inner ones (partially constrained), which is the cause of the fall of deformation to a value of 0.076 mm at node 43 (normalized distance 0.69) in Fig. 4.8. For pathway 43→40, the deformation continuously decreases and becomes zero at the mid-plane since the corresponding boundary conditions restrict the X-, Y-, and Z-movements accordingly. When comparing Figs. 4.5 and 4.6, the stress at node 39 is the least among all the three nodes while the deformation of node 39 is the highest. This is because; node 39 is located on the outermost edge of the quarter gear. As there is no constraint for node 39 to move freely in the radial direction, the stress at node 39 would be the minimum and the corresponding deformation of node 39 would be the maximum. From Fig. 4.5, node 1415 has higher stress than that of node 1609 because node 1415 has only one DOF (vertical) while node 1609 has more than one DOFs. The corresponding deformations of the nodes 1415 and 1609 are reflected in Fig. 4.6, where node 1609 shows higher deformation than that of node 1415.

## 4.2 Dynamic Quenching Analysis of a Steel Tube

### 4.2.1 Model Validation

The model is validated by the experimental results as described in Chapter 4 in section 4.1.1.

### 4.2.2 Convergence Study and the Cooling Curve

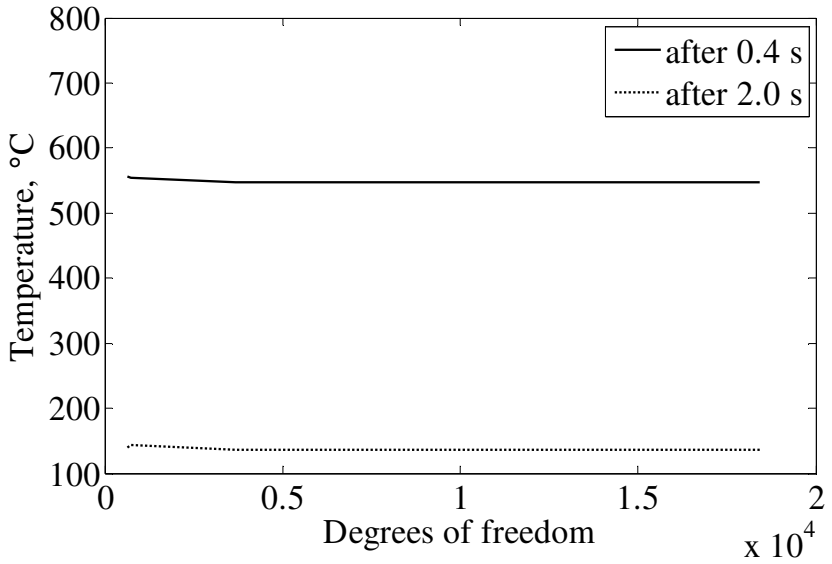


Figure 4.9: Variations of the temperatures of node 24 with degrees of freedom

The variations of the temperature of node 24 (point E of Fig. 3.4) versus the degrees of freedom (DOF) are depicted in Fig. 4.9 for two different time steps; 0.4 s and 2 s. The reason for choosing 0.4 s is because; the major fluctuation of temperature occurs within a very short period of time after the quenching starts. From Fig. 4.9, as the DOF increases, the temperature becomes flattened after showing some initial changes indicating that the solution is already converged and has become mesh independent. Mesh independence studies are done for both the solid FE and CFD models. At first, the CFD model is made mesh independent with the finest element size of 2 mm. Later the FE model is made so with the finest element size of 0.2 mm based on the former.

Figure 4.10 gives the temperature-time history for nodes 2, 24, and 2471 (points J, E, and K, respectively, of Fig. 3.3) quenched by water, whose coordinates are given in Table 3.3. As seen for static analysis in Fig. 4.2, the temperature of each node decreases exponentially with time as the tube cools from 850 °C to 25 °C. All the cooling curves follow the similar trend up to 4 s and are merged after that. It is reasonable to assume that the cooling curves for these three nodes would be of similar shapes for other quenchants but with different cooling rates.

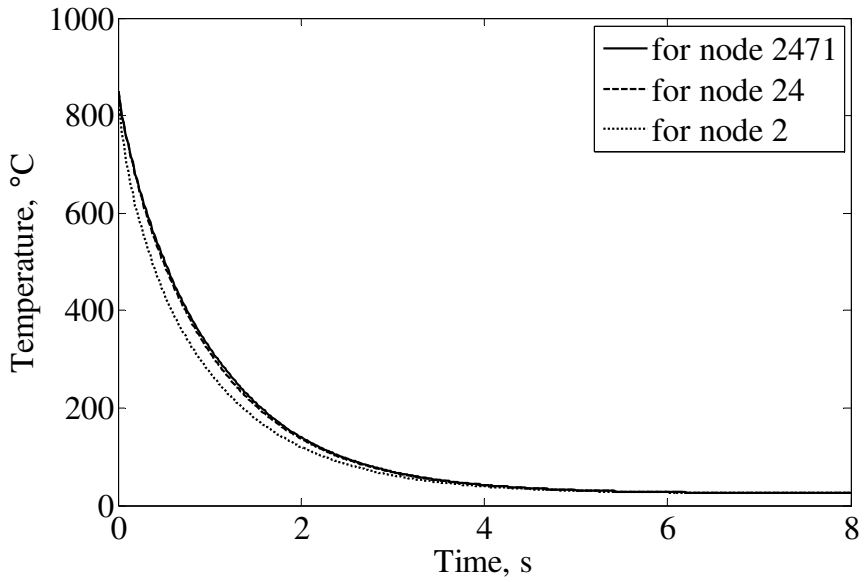


Figure 4.10: Variations of the temperatures of nodes 2, 24, and 2471 with time for water

To compare the cooling capacities for different quenchants, Fig. 4.11 shows the time-varying temperatures of node 24 by water, brine, and PG. The time scale chosen here is logarithmic unlike linear to observe the actual characteristics of the cooling curves. It shows the portion of the cooling curve where the rate of change of temperature (cooling rate or slope of the cooling curve) is very high. Therefore, compared to Fig. 4.10, Fig. 4.11 reveals that rapid cooling of the tube occurs from 0.1 s to 1 s. The time required to cool the tube to the sink temperature is 8 s, 9.5 s, and 8.6 s for water, brine, and PG, respectively. Starting from the same time, the

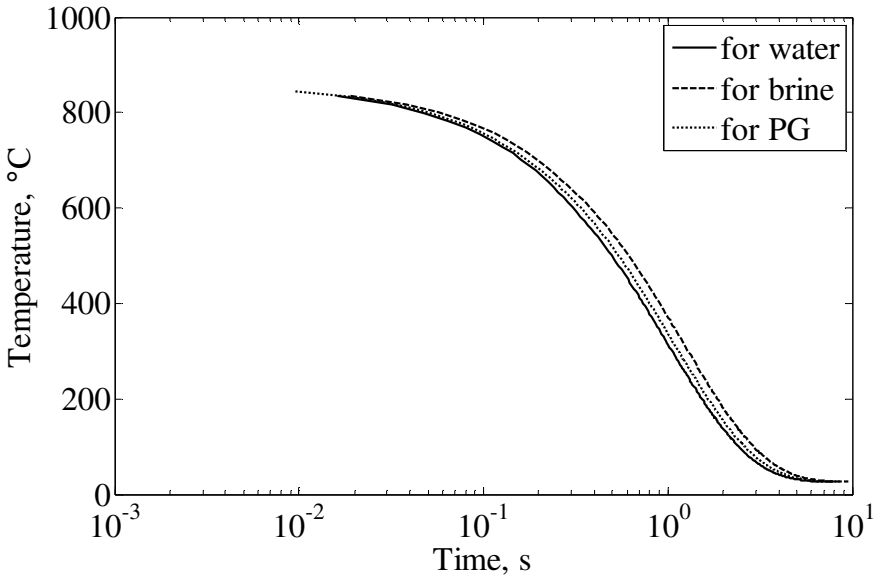


Figure 4.11: Variations of the temperatures of node 24 with time for different quenchants

cooling curve for brine is always above that of water indicating less cooling capacity than water while PG maintains a cooling capacity somewhere in between that of water and brine. The concentration of the aqueous solution as a quenchant affects the cooling rate. The properties of the aqueous solution become closer to water as the concentration of the solution becomes lower.

### 4.2.3 Stress and Deformation Analysis

Figures 4.12 through 4.15 describe the deformed contour of the steel tube for water quenching in terms of the von-Mises stress and the deformation. Similar characteristics of the deformed contour of the tube are found for brine and PG also, with only some variations in the magnitudes of the stress and deformation. From Figs. 4.12(a) and 4.12(b), the highest von-Mises stress generated in the tube is 45.95 kPa, which occurs in the lower-half of the outer surface and the mid-internal surface of the tube in the downstream direction of flow. The magnitude of the highest stress is below the yield stress limit of the steel tube. Therefore, it is reasonable to assume that the steel retains its elastic strain-strain behavior throughout the analysis.

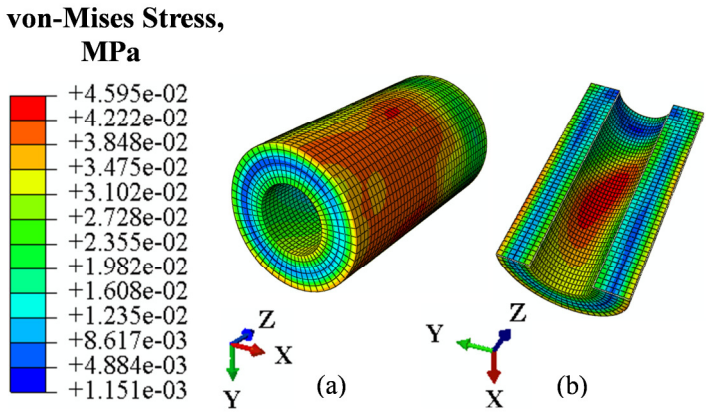


Figure 4.12: Distributions of the von-Mises stresses in (a) the steel tube (b) the cross-sectional half of the tube in the downstream direction of flow

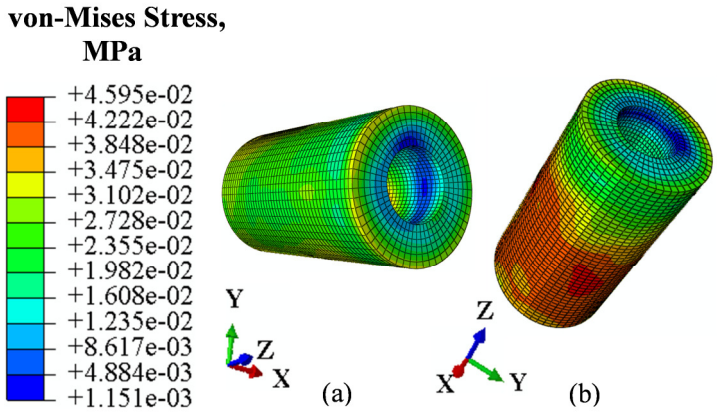


Figure 4.13: Distributions of the von-Mises stresses on outer surface of the tube in (a) the upstream direction (b) the downstream direction of flow

The top surface of the tube shows relatively smaller stress near the vicinity of the internal edge, from Figs. 4.13(a) and 4.13(b). The internal edge in the upstream direction of flow is common to both cooling environments at the top and along the axis of the tube. That is why heat is removed from this edge very fast, but at the same time, temperature of the inner vertical column of the fluid increases as there is no incoming fluid flow. Since, there is always an incoming flow of fluid at the top, the fluid near the vicinity of the top internal edge of the tube has comparatively less temperature than the lower portion of the vertical column of fluid. This produces less temperature gradient between the top internal edge of the tube and the fluid

adjacent to that place, which ultimately causes less stress along the internal edge in the upstream direction of flow. From Fig. 4.13(a), the outer surface of the tube in the upstream direction of flow does not show much variation of stress and the intensity of stress is medium on that surface. This is because the cooling environments in the upstream and in the downstream directions of the tube are different. The bottom surface of the tube is not subjected to the cooling environment. Therefore, the heat conducted upwards from the bottom surface is rapidly taken away from the upstream-side outer surface by the continuously incoming fluid flow. But for the downstream-side outer surface, no incoming flow is there; hence, the cooling intensity is less on that surface compared to the former. This ultimately causes different stress distributions on that surface. The bottom surface of the tube shows low stress level in between the inner and the outer edges of the tube, as this surface is not radially constrained to move.

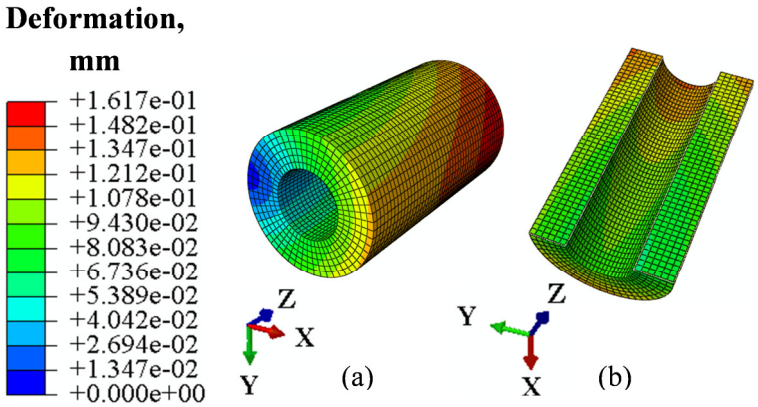


Figure 4.14: Distributions of the deformations in (a) the steel tube (b) the cross-sectional half of the tube in the downstream direction of flow

From the deformation contour of the tube depicted in Fig. 4.14(a), the deformation on the outer surface of the tube in the downstream direction of flow varies axially from bottom to top with the maximum value of deformation at the top. Figs. 4.14(b), 4.15(a), and 4.15(b) show that the high deformation generated on the top surface along positive X-direction gradually reduces

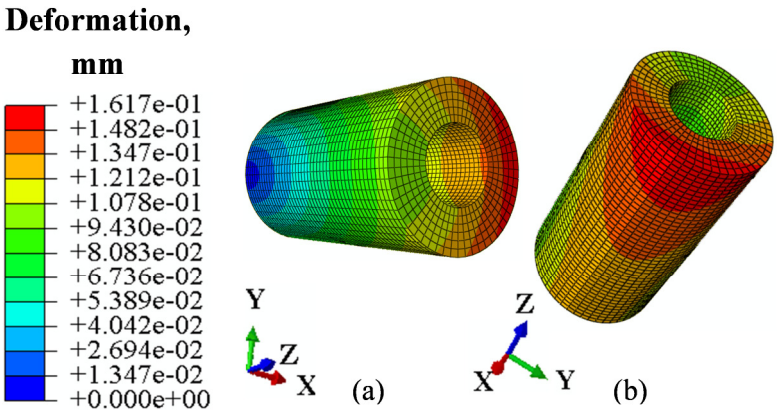


Figure 4.15: Distributions of the deformations on outer surface of the tube in (a) the upstream direction (b) the downstream direction of flow

axially downwards for both the inner and the outer curved surfaces located in the downstream direction of flow. This is because; the top surface of the tube is comparatively free to move vertically than the bottom surface, where the XY-plane is constrained to have no deformation in the Z-direction. The magnitude of the highest deformation generated in the tube is 0.162 mm. From Fig. 4.15(a), the deformation on the outer surface of the tube along negative X-direction also gradually reduces vertically downwards as explained before. Fig. 4.14(a) reveals that the least deformation occurs at the fixed point A described in Fig. 3.2 and Table 3.5. The distribution of the deformation on the outer surface of the tube in the downstream direction of flow is parabolic as represented by Fig. 4.15(b).

### 4.2.4 Time-varying Nodal Stress and Deformation

The time-varying behaviors of the von-Mises stresses at node 24 for all the quenchants are plotted in Fig. 4.16. Starting from zero, all the curves for water, brine, and PG follow a sharp rise of stresses up to 25.6 MPa, 21.4 MPa, and 25.63 MPa within 0.02 s, 0.02 s, and 0.0086 s, respectively. After that, all of them start decaying from the peak stresses exponentially and get flattened, ending with stress values of 8 kPa, 7.71 kPa, and 3.71 kPa for water, brine, and PG,

respectively. As the temperature in the tube gets closer to the sink temperature with time, the magnitudes of stresses become smaller. Initially, the stress level generated by water is higher than that of brine and PG up to around 0.67 s and after that, brine starts generating higher stress than water and PG. However, PG generates the least stress level after 0.67s among all the quenchants.

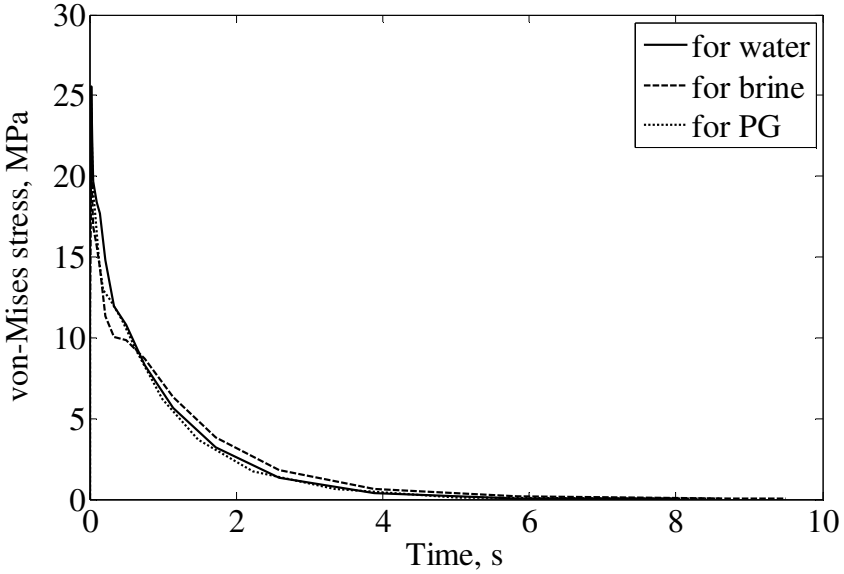


Figure 4.16: Variations of the von-Mises stresses of node 24 with time for different quenchants

The variations of the deformations at node 24 with time for different quenchants are explained in Fig. 4.17. All the water, brine, and PG deformation curves start rising from zero at almost similar rates up to 0.02 s. After that, the gap between the deformation curves for water and brine increases with the water deformation curve at the top of brine, indicating that the water quenching generates more deformation than that of brine. This is expected, since water offers faster cooling than brine and hence, greater quench severity by water creates comparatively higher deformation in the tube. Among all the quenchants, PG shows the least and almost leveled deformation of 0.06 mm after 3.34 s. Comparing Figs. 4.16 and 4.17, a trend of decreasing stress in Fig. 4.16 is counter parted by increasing deformation in Fig. 4.17.

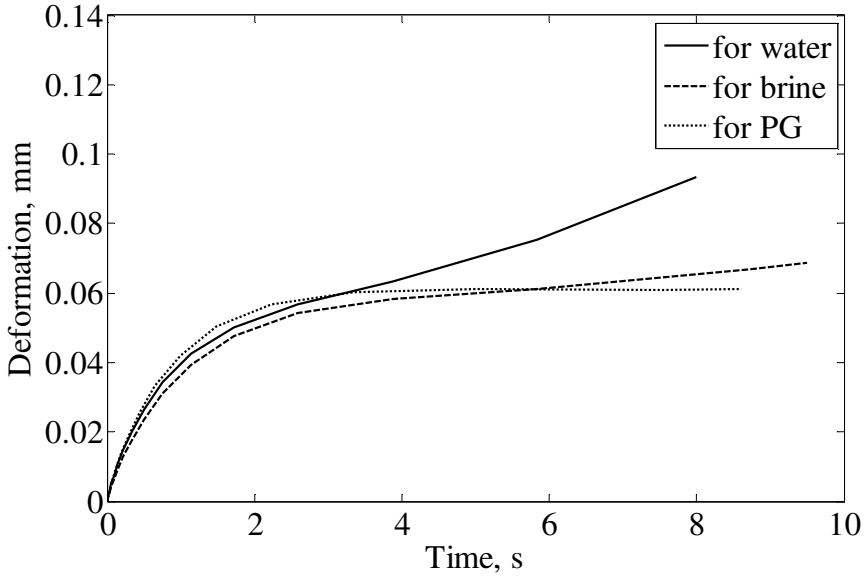


Figure 4.17: Variations of the deformations of node 24 with time for different quenchants

### 4.2.5 Distribution of the Axial Stress and Deformation in the Tube

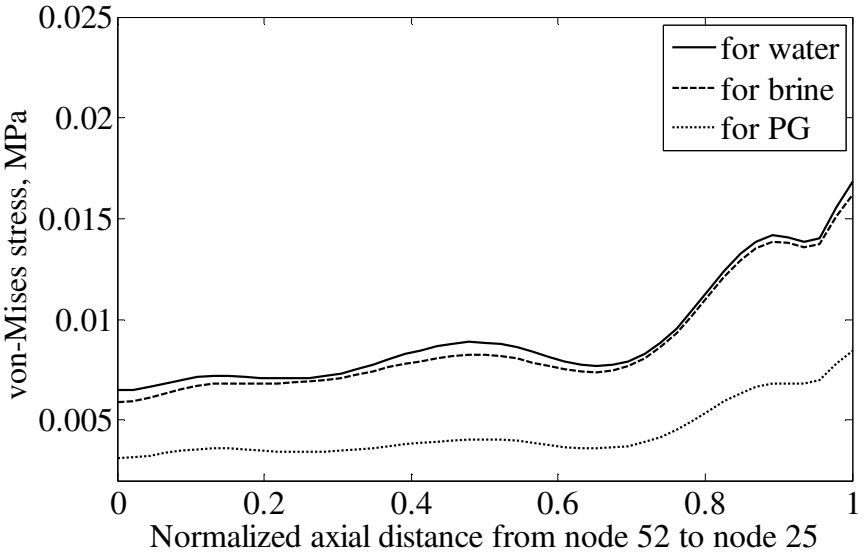


Figure 4.18: Variation of the von-Mises stresses axially along path AB from node 52 to node 25

The variations of the von-Mises stress and the deformation along axial path AB (Fig. 3.3) from node 52 to node 25 are analyzed in Figs. 4.18 and 4.19, respectively. From Fig. 4.18, the stress along path AB from node 52 to 25, including all the nodes within the pathway, fluctuates

harmonically along the whole path but the overall trend gives the information that the stress increases along the path. The level of stress for water is higher than that of brine as before and PG gives the least stress among all of them. The magnitude of the stress generated at the end point of path AB, i.e., at point B is 16.8 kPa, 16.2 kPa, and 8.47 kPa for water, brine, and PG, respectively.

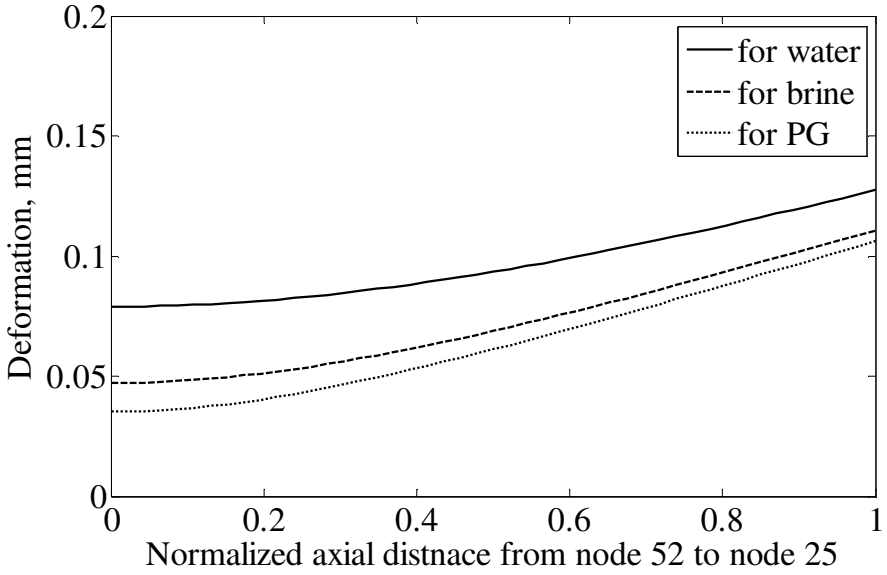


Figure 4.19: Variations of the deformations axially along path AB from node 52 to node 25

From Fig. 4.19, similar characteristics to the axial stress distributions explained above are found when analyzing the axial variation of the deformation in the tube along path AB. The deformations along the axial path increase from point A to point B, i.e., from node 52 to node 25 for all the quenchants. The increase of axial deformation is logical since the higher the position of the nodes from A, the freer the nodes are to move. They do not have any constraint to move vertically unlike the bottom surface of the tube and hence, experience more deformation. Here also, the magnitude of the deformation generated by water quenching is greater than that of brine and PG quenching throughout the axial path. However, PG generates the least axial deformation among all. From Fig. 4.19, the magnitudes of deformations at point A by water, brine, and PG are

0.078 mm, 0.047 mm, and 0.035 mm, respectively, and for point B, they are 0.127 mm, 0.110 mm, and 0.106 mm, respectively.

### 4.2.6 Distribution of the Radial Stress and Deformation in the Tube

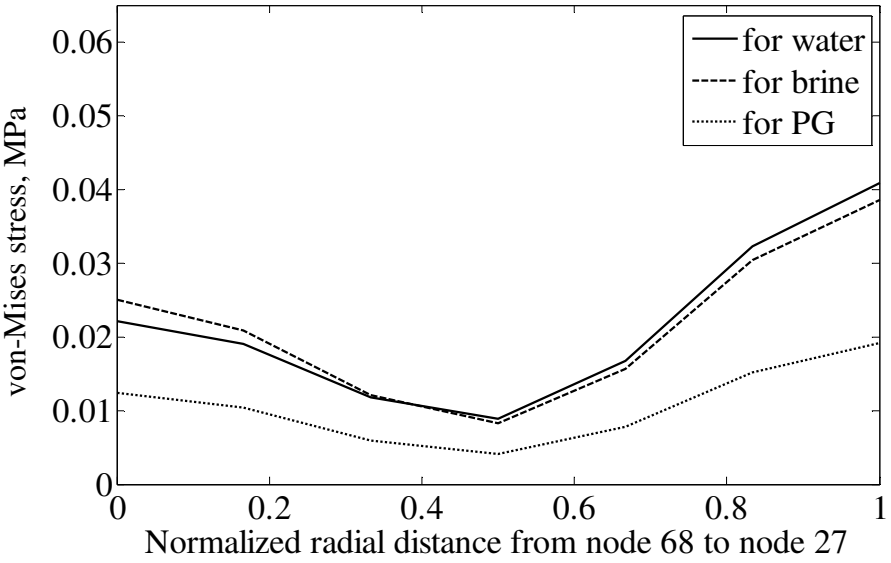


Figure 4.20: Variations of the von-Mises stresses radially along path CD from node 68 to node 27

Figure 4.20 gives the variation of the von-Mises stress along the radial path CD (Fig. 3.3) from node 68 to node 27. Unlike the axial stress distribution, it shows a gradual decrease of stresses from node C to node E for all the quenchants. The magnitudes of stresses on the internal side of the tube at node C are 22.12 kPa, 25 kPa, and 12.47 kPa for water, brine, and PG, respectively, which are 8.86 kPa, 8.24 kPa, and 4.06 kPa for water, brine, and PG, respectively, at the normalized distance of 0.5 at node E. After reaching the lowest stress value at point E, i.e., the midpoint of the radial path, the magnitudes of the stresses start rising again from node E to node D and end up with values of 40.9 kPa, 38.6 kPa, and 19.24 kPa for water, brine, and PG, respectively. The stress level of brine is over that of water up to the normalized distance of 0.4. After that, the stress curve for water is always over the stress curve for brine indicating greater

radial stress level generated by water quenching than brine. Overall, among all the quenchants, PG developed the least radial stress throughout the path.

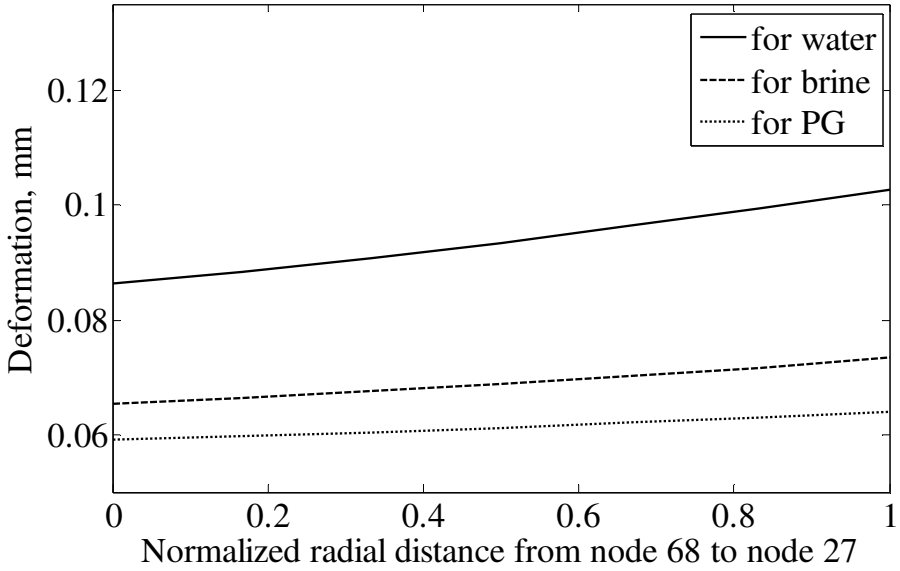


Figure 4.21: Variations of the deformations radially along path CD from node 68 to node 27

Lastly, the variations of the deformations along the radial distance CD are outlined for all the quenchants in Fig. 4.21 where water and PG produce the highest and the least deformations, respectively, among all the quenchants while brine is in the middle. For point C, at node 68, the magnitudes of the deformations generated by water, brine, and PG quenching are 0.086 mm, 0.065 mm, and 0.059 mm, respectively. The slopes of the deformation curves are almost similar up to the normalized distance of 0.2. After that, the slope for the water deformation curve becomes slightly higher than that of brine. Brine also provides a small increase in the slope of the deformation curve compared to PG. However, all curves show that the deformations increase throughout the radial path from node C to node D. This is because the outer surface of the tube is freer to deform radially than the inner surface of the tube due to the difference in the cooling intensities between these surfaces. As the bottom surface of the tube is not subjected to convection, the heat transported from the hot bottom surface towards the outer surface by

conduction is taken away by the side flow of the fluid at a faster rate than that for the inner surface, where the fluid in touch is stagnant. Therefore, the outer surface of the tube shrinks more compared to the inner surface which is obvious from the deformation curve in Fig. 4.21. The magnitudes of the deformations generated on the outer surface of the tube at a normalized distance of 1 at node D are 0.1 mm, 0.073 mm, and 0.064 mm for water, brine, and PG, respectively.

# 5. Conclusions

## 5.1 Static Quenching Analysis of a Spur Gear

Because of the symmetry about the X-, Y-, and Z-axes, a finite element model is developed for a quarter of a steel spur gear to observe the quenching characteristics in terms of residual stress and deformation. Therefore, it is reasonable to assume that the values of the estimates of the remaining part of the full gear would be just the mirror value of the present estimates about the respective axes. The following conclusions are drawn from this investigation:

1. The highest residual stress generated is 248 MPa, which is the plastic yield stress limit of the gear. This stress is generated from the inner side of the gear up to the root circle. However, the intensity of stress is the lowest at the tooth tip. Starting from the tooth tip to the tooth root, the stress is on the increase. Therefore, the critical region for the gear is the portion of the quarter gear radially covering the area from the inner bore edge to the tooth root.

2. The intensity of deformation gradually reduces vertically from the top plane to the bottom plane. However, it increases radially from the inner bore edge to the periphery of the outer circle of the gear and is very high from the start of the involute to the tip of the tooth with the peak value of 0.128 mm. This means that the area of the tooth where the deformation is the maximum has also the minimum stress. The critical region in terms of deformation in the quarter gear covers the area starting from the middle of the tooth to the tip of the tooth. The maximum deformation occurs at the tip of each tooth on the top plane.

3. The behavior of the stress and deformation in the gear mostly depends on the nature of the boundary conditions and constraints (if there is any). If the boundary condition is such that

the gear is relatively free to shrink while quenching occurs, the severity of the thermal stress would be less. Because, in that case, the highest stress developed in the gear does not exceed the yield point.

4. To ensure less stress and deformation, the curvature of the gear needs to be reduced and the sharp edges of the key slots are recommended to avoid as much as possible. The key slots in the gear if possible, should be filleted to avoid large distortions after quenching.

5. The average cooling rate of quenching is calculated simply by dividing the total temperature difference between the gear and the sink with the total time required for cooling and is found to be 27.5 °C/s.

## 5.2 Dynamic Quenching Analysis of a Steel Tube

A three-dimensional fluid-structure interaction model is created for a cylindrical steel tube with different liquid quenchants, where the steel tube constructed as a finite element model is coupled with the liquid quenchant developed as a computational fluid dynamics model for investigating the quenching characteristics in the tube. Three liquid quenchants namely water, brine, and propylene glycol are used to observe the temperature distribution, thermal stress, and deformation in the steel tube. In general, one of the variables in the quenching process that determines the quenching characteristics is the quench severity. Quench severity refers to the ability of a quenchant or a quenching system to extract heat from a sample or a workload during quenching. It is determined either by measuring its hardening power or by measuring its cooling power. The method based on the cooling power includes the analysis of the cooling curve for a quenchant to understand the quenching mechanism. Quench severity of water is greater than that of brine and propylene glycol, as water quenching time is the least among all. The intensities of

the stress and the deformation generated by water quenching are the greatest among all the quenchants. However, it does not necessarily mean that higher quench severity always creates higher stress and deformation in the specimen after quenching. After water, the second highest quench severity applies to propylene glycol due to its higher thermal conductivity and specific heat than brine but still propylene glycol generates the least residual stress and deformation among all the quenchants. The explanation suggests that besides quench severity, there are other important quenching parameters that greatly affect the quenching characteristics. Of them, two important parameters are the wetting property and the viscosity of the quenchants. The least stress and deformation generated by propylene glycol are due to its more uniform wetting property as a polymer compared to water and brine. Moreover, the viscosity of propylene glycol is almost the same as that of brine but higher than that of water, which creates relatively slower and uniform cooling compared to that of water. Considering all the aforesaid features, following outcomes are generalized from this analysis:

1. When considering the cooling capacity, water is better for its least quenching time compared to brine and propylene glycol. But as a quenchant, propylene glycol is better than water and brine as it offers moderate quench severity as well as generates the least residual stress and deformation. In summary, the selection of a suitable quenchant depends on the required quench severity, the wetting property, and the viscosity of the quenchant including the shape, dimension, and composition of the object to be quenched.

2. The highest stress generated in the tube is on the lower-half of the outer surface and on the inner surface of the tube in the downstream direction of flow which is below the yield stress limit of the steel tube.

3. The deformation is the maximum at the outermost edge on the top surface of the tube in the downstream direction of flow along the positive X-axis. The distribution of deformation on the outer surface of the tube in the downstream direction of flow is parabolic vertically downwards from that location.

4. The average cooling rate of the quenchants for the tube is calculated simply by dividing the total temperature difference between the tube and the sink by the total cooling time required for individual quenchants. The average cooling rates for water, propylene glycol, and brine are 103.1 °C/s, 95.93 °C/s, and 86.84 °C/s, respectively; meaning that water quenching rate is 7.47% and 18.72% higher than that of propylene glycol and brine, respectively. The cooling rate of a quenchant should be sufficiently high while maintaining as much uniform cooling as possible.

5. The purpose of the quenching process is to cool the specimen very quickly so that the desired microstructure is developed in the specimen within this short period of time. In that sense, a faster cooling is always preferred. While a faster cooling generates more residual stress and deformation in the specimen, an optimization among different quenchants with different cooling properties is required to allow the specimen to be carefully designed at critical regions. The objective is to ensure the minimum residual stress and deformation by using a suitable quenchant to maintain a balance among achieving desired material properties and other design parameters.

# REFERENCES


[1] Manna, R., "Time-Temperature-Transformation (TTT) Diagrams," p. 9, http://www.msm.cam.ac.uk/phase-trans/2012/Manna/Part2.pdf.

[2] Elkatatny, I., Morsi, Y., Blicblau, A. S., Das, S., and Doyle, E., 2002, "Numerical Analysis and Experimental Validation of High Pressure Gas Quenching," International J. of Thermal Sciences, 42(4), pp. 417–423.

[3] Totten, G. E., Bates, C. E., and Clinton, N. A., 1993, Handbook of Quenchants and Quenching Technology, ASM International, Materials Park, OH.

[4] Jintang, Y., Haiduan, Q., Gongfa, L., and Xiaoliang, Z., 2010, "Numerical Simulation of the Quenching Process of U71Mn Rail-Head Based on ANSYS Software," Proc. of the International Conference on Measuring Technology and Mechatronics Automation, Washington, DC, 2, pp. 811–816.

[5] Toparli, M., and Aksoy, T., 1991, "Calculation of Residual Stresses in Cylindrical Steel Bars Quenched in Water from 600 °C," Proc. of AMSE Conference, New Delhi, India, 4, pp. 93–104.

[6] Sen, S., Aksakal, B., and Ozel, O., 2000, "Transient and Residual Thermal Stresses in Quenched Cylindrical Bodies," International J. of Mechanical Sciences, 42(10), pp. 2013–2029.

[7] Bodede, O. R., Ojo, P. O., Ayodele, O. R., Owa, A. F., and Ajayi, O. B., 2011, "Evaluation of As-Quenched Hardness of 1.2% Carbon Steels in Different Quenching Media," J. of Emerging Trends in Engineering and Applied Sciences, 3(1), pp. 127–130.

[8] Bautista, B., Diaz, D., and Garcia, H., 1992, "Conversion and Use of Polymer Quenchants in Integral Quench Furnace Applications," Proc. of the First International Conference on Quenching and Control of Distortion, Chicago, Illinois, p. 283.

[9] Yamada, K., 1988, "Transient Thermal Stresses in an Infinite Plate with Two Elliptic Holes," J. of Thermal Stresses, 11(4), pp. 367–379.

[10] Wang, H. S., and Chou, T. W., 1985, "Transient Thermal Stresses Analysis of a Rectangular Orthotropic Slab," J. of Composite Materials, 19(5), pp. 424–442.

[11] Fa-rong, Y., and Shang-li, W., 1985, "Transient Temperature and Residual Stress Fields in Axisymmetric Metal Components after Hardening," J. of Material Science and Technology, 1(10), pp. 851–856.

[12] Li, Z., Grandhi, R. V., and Srinivasan, R., 2006, "Distortion Minimization During Gas Quenching Process," J. of Materials Processing Technology, 172(2), pp. 249–257.

[13] Gurney, T. R., 1971, "Residual Stresses in a Large Circular Disc Caused by Local Heating and Cooling at its Centre," J. of Strain Analysis for Engineering Design, 6(2), pp. 89–98.

[14] Schröder, R., 1985, “Influences on Development of Thermal and Residual Stresses in Quenched Steel Cylinders of Different Dimensions,” J. of Material Science and Technology, 1(10), pp. 754–764.

[15] Fletcher, A. J., and Lewis, C., 1985, “Effect of Free Edge on Thermal Stresses in Quenched Steel Plates,” J. of Material Science and Technology, 1(10), pp. 780–785.

[16] Kamamoto, S., Nishimori, T., and Kinoshita, S., 1985, “Analysis of Residual Stress and Distortion Resulting from Quenching in Large Low-Alloy Steel Shafts,” J. of Material Science and Technology, 1(10), pp. 798–804.

[17] Wang, K. F., Chandrasekar, S., and Yang, H. T. Y., 1997, “Experimental and Computational Study of the Quenching of Carbon Steel,” J. of Manufacturing Science and Technology, 119(3), pp. 257–265.

[18] Landau, H. G., Weiner, J. H., and Zwicky, Jr., E. E., 1960, “Thermal Stress in a Viscoelastic-Plastic Plate with Temperature Dependent Yield Stress,” J. of Applied Mechanics, 27(2), pp. 297–302.

[19] Xiao, B., 2010, “Numerical Modeling and Experimental Investigation for Optimization in Quenching Processes of Aluminum and Steel Parts,” Ph.D. Dissertation, Worcester Polytechnic Institute.

[20] Sedighi, M., and McMahon, C. A., 2000, “The Influence of Quenchant Agitation on the Heat Transfer Coefficient and Residual Stress Development in the Quenching of Steels,” Proc. of the Institution of Mechanical Engineers, Part B: Journal of Engineering Manufacture, 214(7), pp. 555–567.

[21] Li, P., Maijer, D. M., and Lindley, T. C., 2007, “Simulating the Residual Stress in an A356 Automotive Wheel and its Impact on Fatigue Life,” Metallurgical and Materials Transactions B, 38(4), pp. 505–515.

[22] Newman, M. L., Robinson, B. J., Sehitoglu, H., and Dantzig, J. A., 2003, “Deformation, Residual Stress, and Constitutive Relations for Quenched W319 Aluminum,” Metallurgical and Materials Transactions A, 34(7), pp. 1483–1491.

[23] Henriksen, M., Larson, D. B., and Van Tyne, C. J., 1992, “On the Analysis of Distortion and Residual Stress in Carburized Steels,” J. of Engineering Materials and Technology, 114(4), pp. 362–367.

[24] Prantil, V. C., Callabresi, M. L., Lathrop, J. F., Ramaswamy, G. S., and Lusk, M. T., 2003, "Simulating Distortion and Residual Stresses in Carburized Thin Strips," J. of Engineering Materials and Technology, 125(2), pp. 116–124.

[25] Li, K., Xiao, B., and Wang, Q., 2009, "Residual Stresses in as–Quenched Aluminum Castings," SAE International J. of Materials & Manufacturing, 1(1), pp. 725–731.

[26] Rose, A., Kessler, O., and Hoffmann, F., 2006 "Quenching Distortion of Aluminum Castings–Improvement by Gas Cooling," J. of Material Science and Engineering Technology, 37(1), pp. 116–121.

[27] Li, M., and Allison, J. E., 2007, "Determination of Thermal Boundary Conditions for the Casting and Quenching Process with the Optimization Tool OptCast," Metallurgical and Materials Transactions B, 38B(4), pp. 567–574.

[28] Xiao, B., Rong, Y., and Li, K., 2010, “Experimental Investigation of Residual Stresses in Water and Air Quenched Aluminum Alloy Castings, Proc. of SEM Annual Conference and Exposition on Experimental and Applied Mechanics, Society for Experimental Mechanics Inc., p. 193.

[29] Kavalco, P. M., Canale, L. C. F., and Totten, G. E., 2009, “Quenching of Aluminum Alloys: Cooling Rate, Strength, and Integranular Corrosion,” Heat Treating Progress, 9(7), pp. 25–30.

[30] Mitchell, I., 2004, “Residual Stress Reduction During Quenching of Wrought 7075 Aluminum Alloy,” Master’s Thesis, Worcester Polytechnic Institute.

[31] Boston Gear, Literature Portal, Catalog, 2003, www.bostongear.com/litportal/pdfs/P-1485- BG_pg289-292.pdf.

[32] The Involute Curve, Drafting a Gear in CAD and Applications, www.cartertools.com/involute.html.

[33] Abaqus, Software Package, SIMULIA, Providence, RI. USA.

[34] Precision Bushings, Acme Industrial Company, Carpentersville, IL 60110.

[35] White, F. M., 2005, Viscous Fluid Flow, McGraw-Hill Companies.

[36] Stoecker, W. F., 1998, Industrial Refrigeration Handbook, McGraw-Hill Companies, pp. 654–655.

[37] Thermo-physical Properties of Brines, 2011, M. Conde Engineering, pp. 6–8.

# VITA

The author was born in the city of Kishoreganj, Bangladesh and passed his early school and college years in Dhaka, Bangladesh. He obtained his Bachelor's degree in Mechanical Engineering in 2007 from Bangladesh University of Engineering and Technology. After graduation, he joined Karnaphuli Fertilizer Company (KAFCO) in Chittagong, Bangladesh and served there up to April 2011 as a Mechanical Maintenance Engineer. He joined Primeasia University in the Textile Engineering Department in June 2011 and worked as a lecturer for almost one year. In the Spring 2013, he joined the University of New Orleans to pursue a Ph.D. in Engineering and Applied Science and continuing there up to now.